DOI: https://doi.org/10.2138/am-2020-7006

Revision 2

Title

Talc CPO determined by improved EBSD procedure for sheet silicates: Implications for anisotropy at the slab–mantle interface due to Si-metasomatism

Author list

Takayoshi NAGAYA [1, 2, 3 *], Atsushi OKAMOTO [3], Ryosuke OYANAGI [3, 4], Yusuke SETO [5], Akira MIYAKE [6], Masaoki UNO [3], Jun MUTO [7], Simon R. WALLIS [1, 8]

[1] Department of Earth and Planetary Science, University of Tokyo, Hongo 7-3-1, Bunkyo, Tokyo 113-0033, Japan. E-mail address: tnagaya@eps.s.u-tokyo.ac.jp

[2] Department of Earth Sciences, University of Southern California, Los Angeles, California 90089-0740 USA.

[3] Graduate School of Environmental Studies, Tohoku University, Aramaki-Aza-Aoba 6-6-20, Aoba-ku, Sendai 980-8579, Japan.

[4] Department of Solid Earth Geochemistry, Japan Agency for Marine-Earth Science and Technology (JAMSTEC), Yokosuka 237-0061, Japan.

[5] Department of Planetology, Graduate School of Science, Kobe University, 1-1, Rokkoudai, Nada-ku, Kobe 657-8501, Japan.

[6] Department of Earth and Planetary Science, Faculty of Science, Kyoto University, Kitashirakawa-Oiwake, Sakyo-ku, Kyoto 606-8502, Japan.

[7] Department of Earth Science, Tohoku University, Sendai, Japan, Aramaki-Aza-Aoba 6-3, Aoba-ku, Sendai 980-8577, Japan.

[8] Graduate School of Environmental Studies, Nagoya University, Furo-cho, Chikusa-ku, Nagoya 464-8601, Japan.

*Postal address: Department of Earth and Planetary Science, University of Tokyo, Hongo 7-3-1, Bunkyo, Tokyo 113-0033, Japan.

E-mail address: tnagaya@eps.s.u-tokyo.ac.jp

Abstract

Talc is widely distributed over the Earth's surface and is predicted to be formed in various tectonic settings. Talc is a very soft and anisotropic sheet silicate showing very low friction behavior. Therefore, the formation of talc is expected to weaken the strength of talc-bearing rocks and may be associated with the initiation of subduction, and with a decrease in the coupling coefficient resulting in aseismic movements along faults and shear zones within subduction zones. For these reasons, understanding the crystallographic preferred orientation (CPO) of talc is important in order to quantify the anisotropy and physical properties of the host rock. However, it is difficult to measure a significant number of talc crystal orientations and to evaluate the accuracy of the measurements using EBSD. Therefore, talc CPO has not been reported, and there is uncertainty regarding the estimation of the strength of deformed talc-bearing rocks. Using methods developed for antigorite, we report the first successful EBSD measurements of talc CPO from a talc schist formed due to Si-metasomatism of ultramafic rocks by subduction zone fluids. We used a combination of W-SEM and FE-SEM measurements to examine domains of various grain sizes of talc. In addition, we used TEM measurements to evaluate the accuracy of the EBSD measurements and discuss the results of talc CPO analysis. Talc CPO in the present study shows a strong concentration of the pole to the (001) plane normal to the foliation. The strongest concentration of the [100] direction is parallel to the lineation. The talc schist produces similar S-wave splitting and P- and S-wave anisotropy as antigorite schist in deeper domains, thus identifying talc-rich layers in subduction zones may require a combination of geophysical surveys, seismic observations and anisotropy modeling. The presence of strong talc CPO in rocks comprising the slab–mantle interface boundary may promote spatial expansion of the slip area during earthquakes along the base of the mantle wedge.

Key words

Talc, Crystallographic preferred orientation (CPO), Electron-backscatter diffraction (EBSD), Si-metasomatism, Anisotropy, Sheet silicates, Seismic observations, Aseismicity

Main Text

1. Introduction

Talc is a common mineral found in ultramafic igneous rocks, metamorphic rocks, and can be formed by alteration (e.g. hydration of dolomite or carbonation of serpentine) and dehydration of serpentine. In addition, talc is thought to be formed at the slab–mantle interface in subduction zones due to metasomatism of the wedge mantle by SiO_2-rich aqueous fluids derived from the subducting slab (e.g., Platt 1975; Brown et al. 1982; Peacock 1987;

Sorensen 1988; Grove and Bebout 1995; Peacock and Hyndman 1999; Och et al. 2003; Fitzherbert et al. 2004; Maekawa et al. 2004; Fotoohi Rad et al. 2005; King et al. 2006; Miller et al. 2009; Escuder-Viruete et al. 2011; Pabst et al. 2012; Bebout and Penniston-Dorland 2016). In addition, talc-rich rock can be formed due to Si-metasomatism during seafloor alteration of mantle rocks (e.g., Lupton 1979; Lonsdale et al. 1980; Allen and Seyfried 2003; Escartín et al. 2003; D'Orazio et al. 2004; Morishita et al. 2009; Marchesi et al. 2013). Talc is stable even at relatively high temperatures when compared to related clay minerals such as smectite (e.g., Moore and Rymer 2007). The dehydration breakdown of talc to enstatite and quartz is predicted to occur at up to ~780–830 ºC (e.g., Bose and Ganguly 1995; Spear 1995) meaning that in subduction zones talc schist will in general be stable for most of the depth range covered by the slab-mantle boundary present in the forearc region (e.g., Escartín et al. 2008). Talc is also predicted to exhibit a low frictional behavior related to the weak bonding in the *c*-axis direction (Moore and Lockner 2004). A number of experimental studies have shown that talc has the lowest friction coefficient, μ, of approximately 0.05 to 0.2, of any of the generally weak hydrous minerals distributed in the wedge mantle (e.g., Moore and Lockner 2007, 2008; Escartín et al. 2008; Viti 2011; Ulian et al. 2012; Hirauchi et al. 2013, 2016, 2019; Kawai et al. 2015). In common with other phyllosilicate minerals, talc commonly show a strong alignment in natural samples. The alignment of the (001) plane of talc may cause the development of a strong anisotropy in a wide range of rock properties along plate boundaries including electrical and thermal conductivities (Guo et al. 2011; Yoneda et al. 2012) and frictional properties (e.g., Mainprice et al. 2008). In addition, the development of a layer of strongly aligned talc is expected to lead to strong permeability anisotropy in a weak

DOI: https://doi.org/10.2138/am-2020-7006

hydrous layer above the subducting slab, which can result in 3D fluid migration in subduction zones and variation in the average slip rate of short-term slow slip events along the strike direction of the slab (Morishige et al. 2017).

However, the crystallographic preferred orientation (CPO) of talc developed in subduction zone plate boundaries is not well known hindering the development of a quantitative understanding of the anisotropy in this area.

The measurement of crystal orientations of a wide range of minerals has been greatly facilitated by the use of electron-backscatter diffraction (EBSD) methods. However, EBSD measurement of hydrous sheet silicates, including talc, antigorite and clay minerals, is challenging for several reasons. 1) Hydrophobic minerals, including talc and antigorite, can be easily damaged by polishing materials during when preparing a thin-section sample making it difficult to polish the sample surface uniformly. In addition, clay minerals can swell during polishing, and mechanically weak hydrous sheet silicates can experience exfoliation along the (001) planes. These factors mean that a sample composed mainly of clay minerals and hydrous sheet silicates must be polished with a small load and a long polishing time in order to avoid damage on the soft surfaces of polished grains and to limit the exfoliation of polished grains from the thin-section surface. 2) In many cases samples consisting of clay minerals and other hydrous sheet silicates are fine grained, and this grain size can be less than the spatial resolution of the most widely used W-SEM-EBSD systems. In addition, the thin-section must be polished thinner for observation using an optical microscope. 3) The detected Kikuchi bands of hydrous minerals tend to be weak, and mis-indexing with other orientations of talc or other minerals can occur. Because of the weak Kikuchi bands produced by clay minerals and hydrous sheet silicates, the presence of a conductive coating commonly used to prevent charging in the SEM can significantly reduce the clarity of the diffraction pattern. Consequently, only a very thin coating can be used, and we need to balance the risk of electric charging on the lightly coated or uncoated sample surface, and the operation time of the SEM observations and EBSD mapping.

For the above reasons, the surface condition of the sample and the SEM operating conditions during the EBSD measurements are important for the detection of clear Kikuchi patterns and the effective indexing of hydrous minerals (e.g., Nishii et al. 2011; Padrón-Navarta et al. 2012; Nagaya et al. 2017). Although indexing the orientations of serpentine minerals such as antigorite, and clay minerals, has been considered to be difficult, recent developments in measurement techniques and procedures have significantly improved the raw indexation rate of antigorite obtained by EBSD mapping (e.g., Van de Moortele et al. 2010; Padrón-Navarta et al. 2012, 2015; Brownlee et al. 2013; Nagaya et al. 2014, 2017; Morales et al. 2018). By carefully polishing the thin-section surface and considering the operation conditions of the SEM following procedures developed for antigorite, we successfully measured the CPO of talc using EBSD. In addition, we evaluated the accuracy of the EBSD indexing by comparison with indexing of the same talc grains using focused ion beam (FIB)-transmission electron microscope (TEM) with a high spatial resolution. In the present study, we investigate the CPO pattern of talc at the slab–mantle interfaces in subduction zones from natural talc schists formed due to metasomatism of mantle materials with SiO_2-rich aqueous fluid derived from the subducting slab and propose a reliable procedure to analyze talc crystal orientations obtained by EBSD for calculating talc CPO.

2. Methods

2.1. Sample description

We carried out EBSD mapping for a natural sample from a talc schist layer of up to ~2 m in thickness collected from serpentinized ultramafic blocks in Jade Cove within the Franciscan Complex, California, USA (King et al. 2003; Hirauchi et al., 2019) (Fig. 1). Talc schist in contact with mud-matrix mélange in this area was formed by the infiltration of slab-derived Si-rich hydrous fluids into the mantle wedge (~450–500 ºC) at the slab–mantle interface (King et al. 2003).

King et al. (2003) propose that the ultramafic rocks in Jade Cove originated in the wedge mantle in contact with the subducting slab. In contrast, Hirauchi et al. (2008) concluded that the ultramafic blocks in Jade Cove were originally pieces of detached slabs of abyssal peridotites, which were exposed along oceanic fracture zones near the mid-oceanic ridges. These pieces experienced subduction into the depth of the stability field of antigorite and were subsequently incorporated into the Franciscan subduction complex accompanied by metasomatism. The source rocks of the ultramafic blocks in Jade Cove are thus contentious. In addition, most Franciscan rocks were estimated to be metamorphosed at peak temperatures of less than ~350°C (e.g., Bröcker and Day 1995; Cooper et al. 2011; Schmidt and Platt 2019), which is lower than temperatures at which the serpentinization to antigorite occurs (greater than ~300–400°C) and lower than the temperature of the metasomatic reaction that produces the talc-rich rocks in Jade Cove. This means that the serpentinite blocks, including talc schists in Jade Cove, are exotic ultramafic blocks with different subduction and exhumation histories

DOI: https://doi.org/10.2138/am-2020-7006

from the surrounding Franciscan metagraywacke. Therefore, the SiO_2-rich aqueous fluids related to the metasomatic reaction to form talc schist in Jade Cove may not be derived from the metagraywacke matrix, and the exact origin of the fluids remains unclear. However, we emphasize the possibility that the talc schist used in the present study was formed due to the metasomatic reaction of ultramafic rocks with SiO_2-rich aqueous fluids along the slab–mantle interface at the depth of the stability field of antigorite (~450–500ºC, King et al. 2003) within the subduction zone. While these rocks are currently exposed as exotic ultramafic blocks incorporated into the Franciscan Complex (e.g. Wakabayashi 1992; King et al. 2003; Hirauchi et al. 2008), we use the talc schist collected here because it likely formed as the result of similar processes that occurs at the slab–mantle interface.

Using polarized light microscopy, micro-Raman spectroscopy, X-ray powder diffraction (XRD), and electron probe micro-analyzer (EPMA), we confirmed that the talc schist used in the present study consists mainly of talc (approximately 70 vol.%) with minor tremolite. Minor amounts of clinochlore and calcite are also present (see the next section for measurement conditions). The areas of the talc grains and the long axes of the tremolite grains are up to a few hundred square micrometers and a few hundred micrometers, respectively. In the present study, the foliation, S, is defined by the orientation and grain shape of platy talc and tremolite grains, and the mineral lineation, L, is defined by the preferred orientation of the long axes of tremolite grains. The axes of symmetry of the S–L fabric are taken as corresponding to the principal axes of finite strain in the rock. The minimum stretch (or shortening) direction is perpendicular to S, and the maximum stretch direction is parallel to L. In the EBSD mapping, we used a thin-section sample cut parallel to the foliation.

2.2. Analytical instruments

2.2.1. XRD

In order to determine the mineral assemblage, a powdered sample of the talc schist sample was examined with an X-ray diffractometer (Rigaku MiniFlexII) at Tohoku University, Japan using Cu–Kα radiation and a 2θ step size of 0.02º.

2.2.2. Laser Raman spectrometer and EPMA

Different polished thin-sections from those used in the EBSD and FIB-TEM measurements were prepared from the talc schist sample and analyzed using a laser Raman spectrometer (Horiba XploRa PLUS) with a 532-nm laser connected to a confocal microscope (Olympus BX51) and an EPMA (JEOL JXA-8200) equipped with five wave-length-dispersive X-ray spectrometers at Tohoku University. Thin-section samples for Raman and EPMA measurements were polished using a series of diamond pastes with decreasing grain sizes down to 1/4 micron. For the Raman measurements, an uncoated thin-section sample was used and the Raman signal was dispersed using a 2,400 grooves/mm grating. In the EPMA measurement, a carbon coated thin-section sample was used, and the accelerating voltage, beam current, and focused beam diameter were 15 kV, 12 nA, and 1–2 μm, respectively.

2.2.3. EBSD analysis

Thin-sections for EBSD measurements were polished using a series of diamond pastes with decreasing grain sizes down to 1/4 micron and were further treated with colloidal silica to remove the surface damage zone. In order to avoid damage to and the mechanical removal of the polished surface grains, the polishing loads acting perpendicular to the sample were kept to a minimum during all stages of polishing. To reduce the risk of removal of material by ultrasonic cleaning and removal of carbon and copper conductive tapes applied to the surface, the time for ultrasonic cleaning after each polishing step was kept to a minimized (~5–15 seconds), and well-polished areas were selected after polishing and cleaning for the subsequent analyses. Talc-rich thin-sections can be overly thinned during polishing due to the fine grain size, which results in increased risk of charging in the SEM. As a result, we prepared thicker (~50 μm) thin-sections for EBSD measurements than those used for polarized light microscopy.

Crystal orientations were determined using a scanning electron microscope equipped with an EBSD system (JEOL JSM-6510LV with Oxford HKL Channel5) and an accelerating voltage of 10 kV at Nagoya University. The SEM chamber pressure was a low vacuum (10 Pa), allowing uncoated samples to be used. The SEM magnification during observation and measurement was kept to approximately ×50–60. Low-magnification SEM measurements help to minimize charging issues of uncoated samples and assist in obtaining high-quality EBSD patterns (e.g., Nagaya et al. 2017). For mapping using a step size of less than 1 μm, crystal orientations were determined using a field-emission scanning electron microscope (FESEM) equipped with an EBSD system (JEOL JSM-7001F with Oxford HKL Channel5) at an accelerating voltage of 15 kV at Tohoku University. A sample coated with carbon at a relatively thin thickness of ~10 nm was used for these measurements. This is the minimum coating that will prevent charging at higher kV and not interfere with the diffraction pattern.

In measurements by both FE-SEM-EBSD and W-SEM-EBSD systems, mapping was carried out with automatic indexing using Oxford Instruments Aztec software with 4×4 pixel binning. The minimum and maximum numbers of detected bands in the EBSD patterns were 5 and 12, respectively. The sample stage was tilted by 70° during EBSD mapping.

In EBSD mapping, we used the orientation data of talc and tremolite with MAD values of less than 2.0º. The MAD value expresses the mean angular deviation between the detected and indexed Kikuchi patterns and expresses how well the simulated EBSD pattern corresponds with the actual measured pattern. In order to determine a suitable upper limit for the MAD values used in the calculation of the CPO patterns of talc, we also examined the accuracy of indexing of talc grains by comparing the orientation data filtered using a gradually decreasing MAD value from a maximum of 2.0º.

There are only very small differences between the unit cells for the different crystal systems of talc (monoclinic and triclinic), between those for the different Ca-amphiboles (e.g. tremolite and actinolite), and between those for different databases of talc or Ca-amphiboles. Therefore, the Kikuchi patterns could not be used to distinguish between different possible types of Ca-amphibole and crystal systems of talc. In the present study, we used the crystallographic parameters of talc and tremolite obtained from the monoclinic (*C2/c*) polytype of talc of the Inorganic Crystal Structure Database (ICSD) (a = 5.262 Å, b = 9.102 Å, c = 18.813 Å, and β = 100.08º) and the monoclinic (*C2/m*) polytype of actinolite (Evans and Yang 1998) (a = 9.977 Å, b = 18.287 Å, c = 5.308 Å, and β = 104.81º), respectively, to index the Kikuchi patterns, and software developed by D. Mainprice to calculate the CPOs (Mainprice 1990). For other details of the procedure of sample preparation and EBSD analysis, we followed Nagaya et al. (2017), who describe the procedure applicable to hydrous minerals.

2.2.4. FIB-TEM analysis

TEM measurement of one talc grain was carried out for comparison with the EBSD results. A FIB system (FEI, Quanta 200 3DS) at Kyoto University was used to extract samples of a talc grain from a thin-section prepared parallel to the foliation. A predefined area within the talc grain where EBSD measurements were carried out was coated with Pt, and the surroundings were cut out using a Ga^+ ion gun. The resulting leaf was broken off at its base mechanically and then mounted on a TEM grid. The extracted sample leaves were thinned using a Ga+ ion beam at an accelerating voltage of 30 kV and a beam current of 0.1–30 nA. The samples were studied using a JEOL JEM-2100F TEM operated at 200 kV at Kyoto University. TEM images were recorded using a CCD camera (Gatan, Orius 200D).

A thin membrane was then cut from this grain using FIB milling, and the TEM electron diffraction pattern was used to confirm that the membrane had been cut sub-normal to the talc (001) plane and the crystal system of talc (monoclinic or triclinic). The monoclinic and triclinic talc have similar crystal structures with the only difference being stacking of the (001) planes. TEM observation is effective in confirming the presence or absence of weak diffraction spots due to its high scattering power. The electron diffraction pattern was then used to rotate the sample so that the incident electron beam was normal to the talc (001) plane. The direction parallel to the *a*-axis can then be identified using the electron diffraction pattern.

2.3. Seismic anisotropy calculation

We calculated the seismic anisotropy corresponding to the fabric of the talc schist estimated from the crystal orientation (the Euler angle) data for each mineral obtained from EBSD measurements and the volume ratio of each mineral obtained from the EBSD map and SEM images. In addition, we compared the seismic anisotropy of the talc schist with that of antigorite schist predicted to be widely distributed in the hydrated wedge mantle in order to examine the possibility that talc-rich domains can be distinguished using seismic observations.

In this calculation of the seismic anisotropy of talc and antigorite schists, we used the elastic stiffness coefficients and densities of talc, tremolite and antigorite single crystals obtained from Mainprice et al. (2008), Brown and Abramson (2016) and Bezacier et al. (2010), respectively. For antigorite schist, we used the antigorite crystallographic parameters (a = 43.5852 Å, b = 9.2624 Å, c = 7.2460 Å, and β = 91.160º) and the CPO patterns reported in Bezacier et al. (2010) and Nagaya et al. (2014). We also examined the effect of the talc crystal system on the seismic anisotropy of talc schist based on the measured CPOs of talc and tremolite. In this comparison, we used the database of the crystal structure for the triclinic ($C\bar{1}$) polytype of talc at room pressure, where a = 5.2957 (Å), b = 9.1810, c = 9.4228, α = 90.372º, β = 98.880º, and γ = 90.110º, and the crystal structure for the monoclinic ($C2/c$) polytype of talc at room pressure, where a = 5.2976 (Å), b = 9.1447, c = 18.8083, α = 90º, β = 101.471º, and γ = 90º (Mainprice et al. 2008). In addition, in the estimation of the seismic anisotropy of talc schist at approximately 0.9 GPa, we used values of the crystal structure, density, and elastic coefficients at 0.87 GPa for triclinic talc, and values of the crystal

This is a preprint, the final version is subject to change, of the American Mineralogist (MSA)
Cite as Authors (Year) Title. American Mineralogist, in press.
DOI: https://doi.org/10.2138/am-2020-7006

structure and density at 0.93 GPa and elastic coefficients at 0.96 GPa for monoclinic talc calculated by Mainprice et al. (2008). We also used software developed and published by D. Mainprice for preparation of the figures and the calculation of seismic wave anisotropy (Mainprice 1990). In the present study, we show the calculated seismic anisotropies of Vp, Vp/Vs_1, Vp/Vs_2, dVs, AVs and Vs_1 Polarization for monoclinic and triclinic talc under 0 and 0.9 GPa. Here, Vp (km/s) gives the 3D distribution of the P-wave velocity. The anisotropy of P-waves (AVp) (%) is 100(Vpmax − Vpmin)/[(Vpmax + Vpmin)/2], where Vpmax and Vpmin are the maximum and minimum P-wave velocities in all directions, respectively. In addition, Vp/Vs_1 and Vp/Vs_2 give the 3D distribution of the ratios of the P-wave and fast shear wave (Vs_1) velocities and the P-wave and slow shear wave (Vs_2) velocities, respectively. The anisotropy of Vp/Vs_1 (%) is $100(Vp/Vs_1max - Vp/Vs_1min)/[(Vp/Vs_1max + Vp/Vs_1min)/2]$, where Vp/Vs_1max and Vp/Vs_1min are the maximum and minimum Vp/Vs_1 in all directions, respectively and the anisotropy of Vp/Vs_2 (%) is $100(Vp/Vs_2max - Vp/Vs_2min)/[(Vp/Vs_2max + Vp/Vs_2min)/2]$, where Vp/Vs_2max and Vp/Vs_2min are the maximum and minimum Vp/Vs_2 in all directions, respectively. The 3D distribution of the difference between the fast and slow polarized S-wave velocities ($Vs_1 - Vs_2$) is given as dVs (km/s), and AVs (%) gives the 3D distribution of the polarization anisotropy of S-waves owing to S-wave splitting, $200(Vs_1 - Vs_2)/(Vs_1 + Vs_2)$, where Vs_1 and Vs_2 are the fast and slow polarized S-wave velocities in a given direction, respectively. Furthermore, Vs_1 Polarizations show the polarization directions of the fast S-waves passing through the talc schist in various directions. The AVs and Vs_1 Polarizations can be compared to observations of the delay time and fast direction of the polarized S-waves from a specific direction in modern convergent margins. When considering uncertainties associated with estimates of seismic anisotropy for talc and antigorite schists, we also consider the effect of various averaging schemes (the Voigt (constant strain) and Reuss (constant stress), and the intermediate Voigt-Reuss-Hill averages) used to derive elastic anisotropy from CPO.

3. Results

3.1. Talc CPO and tremolite CPO of metasomatic talc schist in Jade Cove

The talc CPO calculated from EBSD mapping with a step size of 1 μm is shown in Fig. 2. This pattern shows that the strongest concentration of the direction normal to the (001) plane is normal to the foliation, similar to the pattern for other platy minerals, such as antigorite (e.g., Nagaya et al. 2017). The strongest concentration of the *a*-axes is parallel to the lineation, and that of *b*-axes is parallel to the foliation and normal to the lineation. However, both the *a*- and *b*-axes display a bimodal distribution with additional strong concentrations within the foliation at 90º from the maximum concentration.

EBSD mapping with a step size of 500 nm shows the crystal orientations of some talc grains that cannot be indexed in the map with a step size of 1 μm (Fig. 3). In addition, as a result of calculating two talc CPOs from 1) a higher raw indexing rate area (~19%) where continuous indexing points and relatively coarse talc grains are contained (Fig. 3d), and 2) a lower raw indexing rate (~13%) area where indexed talc grains are fine or indexing points within a grain are isolated (Fig. 3e), both CPOs show the same talc CPO pattern as that obtained by EBSD measurement with a step size of 1 μm. This means that in the range of more than 500 nm, there is little change in the talc CPO pattern due to the difference in grain size in the sample and the difference in the raw indexing rate during EBSD mapping.

Tremolite CPO displays a strong concentration of *a*-axes normal to the foliation and the pole to the (001) plane is concentrated parallel to the lineation (Fig. 3). This is consistent with the preferred orientation of tremolite in talc-rich fault rocks, which revealed that the poles to the (001) plane of tremolite are likely to be parallel to the (001) plane of talc and the foliation plane (Viti and Collettini 2009).

However, the EBSD mapping of a single grain of talc where very similar Kikuchi patterns are detected, shows indexing of different crystal orientations of talc. This means that mis-indexing of multiple directions can occur during EBSD mapping of a talc grain. In particular, strong concentrations of *a*- and *b*-axes occur every 30º of rotation on the (001) plane of talc, as shown in Figs. 4 and 5.

3.2. Verification of mis-indexing of talc in EBSD by FIB-TEM analysis

In our sample, we observed EBSD mis-indexing associated with 30º rotations around a pole to the (001) plane of talc (Figs. 4 and 5). It is desirable to find ways to correct mis-indexed orientation data for talc. Such data are particularly common when data associated with relatively high MAD values are used. As a result of comparing the orientation data filtered using gradually decreasing MAD values from a maximum of 2.0º to 0.5º, we found that the directions of the strongest concentrations of *a*- and *b*-axes change when filtered with MAD values of less than 1.5º and 1.3º, respectively (Fig. 5).

In addition, in order to determine appropriate MAD values for filtering in the EBSD measurement of talc, we performed TEM measurements of the crystallographic orientation of a single grain of talc, showing numerous possible orientations when using different values of the MAD filter (Fig. 6). In TEM measurements, the diffraction spots along the *c** direction show a periodicity of ~9.3 Å both in [100] and [010] zone axis patterns (Figs. 6e and 6f). There is no 18.5 Å periodicity which characterizes the monoclinic (*C2/c*) polytype, indicating that the present talc is actually the triclinic ($C\bar{1}$) polytype. Therefore, in the present study, electron diffraction patterns along the [100] and [010] directions are indexed as triclinic ($C\bar{1}$) polytype (density: 2.7758 (g/cm^3), a = 5.29 (Å), b = 9.17 (Å), c = 9.46 (Å), α = 90.46º, β = 98.68º, and γ = 90.09º; Perdikatsis and Burzlaff 1981), although EBSD patterns were indexed as monoclinic (*C2/c*) symmetry. Note, however, that the TEM analyses are probably comparable to the EBSD results in the context of the direction of crystal axes (see section 4.1.2). In addition, streaks on TEM spots can be seen in the *c** direction due to the micro twins and stacking faults. The thickness of talc grains is mainly ≤ ~1 μm (Fig. 6).

4. Discussion

4.1. CPO measurements of talc by EBSD

4.1.1. Sample preparation of hydrous sheet silicates

We successfully indexed Kikuchi patterns from a thin-section of talc schist cut parallel to the *XY*-plane using FE- and W-SEM-EBSD. However, it is difficult to obtain clear Kikuchi patterns from thin-sections cut parallel to the *XZ*- and *YZ*-planes.

This result is consistent with previous results reporting sample preparation problems for soft sheet-structured minerals, such as graphite (hardness: 0.5–1) (Kouketsu et al. 2019), muscovite and chlorite (hardness: 2.5) (Inoue and Kogure 2012). In these mechanically weak sheet silicates, surface damage on thin-sections cut normal to the foliation occurs due to shear in the direction normal to the (001) planes, even when treated with colloidal silica during the polishing process. This surface damage can remain after colloidal silica due to micro-bending of the (001) planes. Antigorite has a hardness of 3 and Nagaya et al (2017) show that Kikuchi patterns can be detected from both thin-section samples parallel and normal to the foliation. TEM observations of antigorite schist do not show the clear damage zone by micro-bending of (001) in thin-sections cut normal to the foliation (Nagaya et al. 2017). Therefore, when using samples composed mainly of mechanically weak sheet silicates with a hardness of less than 3 for EBSD measurements, the best results will be obtained from thin-sections cut parallel to the foliation. In addition to damage during polishing, the thinness of talc grains, < ~1 μm (Fig. 6), may also contribute to difficulties in obtaining clear Kikuchi patterns in thin-sections normal to the foliation.

In contrast, for thin-sections cut parallel to the foliation, the damage zones of the sheet silicates are likely to be parallel to the (001) planes and to be relatively easily removed along the (001) planes due to anisotropic crystalline bond strengths, and mechanical distortion due to micro-bending can be limited in this orientation. The crystal bond strengths are thought to be closely related to the linear bulk moduli and minerals that show a strong crystallographic control on this property are likely to undergo exfoliation in specific orientations. Platy minerals commonly exhibit a linear bulk modulus normal to the (001) plane that is much less than parallel to the same plane; examples of these ratios are ~55–70% for chlorite (e.g. Mookherjee & Mainprice, 2014), 31–45% for antigorite (e.g. Capitani and Stixrude 2012), ~15–21% for muscovite (e.g. Ortega-Castro et al., 2010), ~14–33% for talc (e.g., Stixrude

2002; Gatta et al., 2013) and ~3% for graphite (e.g. Wang et al., 2012). TEM observations of a thin-section parallel to the foliation in the present study are in agreement with these results for antigorite and show no clear surface damage on the talc surface. Therefore, well-polished surfaces of sheet silicates suitable for EBSD measurements are preferentially developed in sections parallel to the foliation, even when using samples composed mainly of mechanically weak sheet silicates with a hardness of less than ~3. In addition, the talc schist used in the present study consists mainly of talc and the contrast of hardness within a thin-section sample is very low, which may make it easy to make a uniformly well-polished surface. However, when making a thin-section of a sample that consists of multiple minerals of different hardnesses, mechanically weak minerals such as talc, brucite and chlorite in antigorite serpentinite, and graphite and muscovite in quartzite can be indented on the thin-section surface relative to the harder minerals. It is not easy to polish these indented portions. In addition, the electron beam cannot reach indented portions of a thin-section because the surface is tilted to 70°. Thus the topography created by differential hardness increases the difficulty in obtaining EBSD patterns from soft minerals, and likely contributes to low raw index rates for soft minerals, even in thin-sections cut parallel to the foliation.

4.1.2. MAD filtering and the quality of resulting EBSD data of talc

The talc in the present study was most often indexed as monoclinic talc. However, it is difficult to distinguish between the crystal systems of talc using EBSD because the mean angular deviations (MADs) between Kikuchi patterns from databases of monoclinic and triclinic talc are only up to 2–3º, which is very near the threshold for acceptance in EBSD indexing of talc (0.5–2.0°). In addition, the number of Kikuchi bands and the magnitude of the crystal structure factor, which are used to index the detected Kikuchi pattern and the determination of the crystal orientation in the EBSD measurement, are also important for the accuracy of the indexing. In general, indexing by EBSD can be controlled by the larger crystal structure factor compared to indexing by TEM. These mean that both databases of monoclinic and triclinic talc have the possibility to be indexed in EBSD measurements unless one of two crystal systems fits the detected Kikuchi patterns with very low angular difference. Therefore, in theory, it is possible to identify the crystal system of talc when the acceptable angular difference between the detected and indexed Kikuchi patterns is very low. However, in this case the indexing rate will also be very low. In addition, the present study shows that talc is identified by EBSD as monoclinic even after filtering using very low MAD values. In contrast TEM measurements identify the talc as triclinic.

In addition to the small angular differences among different crystal systems of talc and among different databases of talc, even if the same database of talc is used, similar diffraction geometries and predicted Kikuchi patterns are simulated when the crystal is rotated around the direction normal to the (001) plane (even in the case of triclinic talc, the values of α and γ are approximately right angles: $(90 - \alpha)^{o}$ or $(90 - \gamma)^{o} < {\sim}0.5^{o}$). Therefore, the mis-indexing of *a*- and *b*-axes of talc rotated around the direction normal to the (001) plane is the most common mis-indexing pattern of talc in EBSD measurement. This is consistent with the case of mis-indexing in EBSD measurements of antigorite, another example of a hydrous sheet-silicate mineral (Nagaya et al. 2017). This earlier study showed that reliable CPO patterns of antigorite were obtained by filtering the data using a maximum mean angular difference between the detected and indexed Kikuchi patterns of 0.7º for measurements normal to the foliation.

Based on the TEM measurements in the present study, the talc grain was identified as triclinic, and its crystal orientation is in close agreement with the orientation shown by EBSD mapping using a relatively low MAD_{max} filtering of 1.3–0.5º (Figs. 5 and 6). This means that differences in crystal systems of talc do not have a significant effect on the resulting CPO irrespective of the crystal system used for EBSD measurement. In addition, this comparison of EBSD results with TEM measurements is consistent with a general understanding that results with lower MAD values are more reliable than those with higher MAD values. However, using an MAD value of less than 0.5º, imposes excessively severe restrictions on the data, and the data accepted for analysis are drastically reduced in number. In our measurements, indexing points with MAD values of less than 0.5º make up approximately 9% of all points with MAD values of less than 2.0º. Limiting the orientation data using excessively low MAD values may lead to selective filtering out of certain crystal directions (Nagaya et al. 2017). Therefore, we propose using an MAD_{max} of 1.3–0.7º for talc CPO analysis of planes parallel to the foliation. For the single grain of talc used in the present study, even if the MAD_{max} filtering of 1.3–0.7º is used some incorrect indexing still occurs (Fig. 5) mainly associated with rotation about the direction normal to the (001) plane. EBSD indexed points in agreement with the TEM measurement within the range of ~20º make up approximately 29% to 32% for the [100] and [010] directions (*a*- and *b*-axes) and approximately 85% to 94% for the direction normal to the (001) plane (sub-normal to *c*-axis) of all points after filtering the data (Table 1). However, the strongest orientations for the [100] and [010] directions and the direction normal to the (001) plane of talc and the overall CPO pattern do not show significant changes when the MAD_{max} filtering criteria is lowered from 1.3º to 0.7° and these orientations are in agreement with the TEM results.

In the present study, the talc CPO could not be obtained from samples normal to the foliation. The EBSD maps of talc (and tremolite) in the large areas (Area 1 in Figs. 2b through 2d and Areas 2 and 3 in Figs. 3b and 3c) show a lower raw indexing rate of ~8–19%, as compared to a raw indexing rate of ~25% within a talc single crystal (Area 5 in Fig. 4b). The EBSD mapping of numerous grains generally shows a lower raw indexing rate due to the grain boundaries and the distribution of minor constituent minerals that are not selected to be indexed, in addition to the grain surfaces of talc (and tremolite) with a damage zone related to the polishing issues. Significant differences in raw indexing rates for different sections (e.g. foliation-parallel versus foliation-perpendicular) raises the possibility that specific orientations are underrepresented in the final CPO due to the combination of (1) poor indexing when EBSD measurements are made for some particular crystal orientations of talc and (2) the strong, crystallographically-controlled grain shape fabric resulting in a greater probability of a particular direction of the talc grains intersecting with the observed section. The strength of Kikuchi patterns may also depend on the orientation of the crystal plane being measured. Therefore, the presence of weak Kikuchi patterns due to the specific crystal orientations may also related to the raw indexing rates and mis-indexing in addition to issues of polishing and measuring conditions and similar EBSD patterns of talc. Even if the crystallographic orientation could not be determined, such specific crystal planes are likely to be observable in the Band Contrast images. Due to the strong relationship between talc grain shape and crystallographic orientation, such grains should also show similar shapes. However, in the present study, we were not able to find non-indexed talc grains with specific grain shapes from BC images (Figs. 2 and 3). An additional concern is the possibility that EBSD measurement using a thin-section parallel to the foliation may show the apparently exaggerated concentration of the (001) planes of the sheet silicates due to the relatively large area of sheet silicates lying at a low angle to the foliation compared to the area of sheet silicates at a high angle to the foliation (e.g., Bachmann et al. 2011; Nagaya et al. 2017; Morales et al. 2018). This matter of concern regarding the geometry between the sample structure and the measurement surface has been problematic when the accuracies of the measurement results for physical properties of sheet silicates are evaluated for the bulk rock seismic velocity and anisotropy obtained from experiments using natural samples (e.g. Ji et al. 2013; Watanabe et al. 2014) and calculated from EBSD data derived from manual indexing (e.g. Nishii et al. 2011), as well as EBSD mapping. However, TEM observations of the plane normal to the foliation of the talc schist in this study show that talc grains lying at a high angle to the foliation are rare (Fig. 6). This is consistent with SEM observations of the talc schist that show it consists of mainly platy planes of talc at a low angle to the foliation (Figs. 3a and 4a). These observations suggest the EBSD talc mapping showing a very strong concentration of (001) planes is a reasonable result.

Regarding the uncertainty of the *a*- and *b*-axes on the (001) plane of sheet silicates, in the case of the antigorite CPOs reported by Nagaya et al. (2017), the CPO obtained from the samples parallel to the foliation of antigorite serpentinite shows the same pattern and strength as the CPO measured from the samples normal to the foliation and filtered using the lower

MAD values (< ~0.7°). In addition, the examples of antigorite show small differences in seismic velocity along the *a*- and *b*-axes when compared to the *c*-axis (Bezacier et al. 2010; Mookherjee and Capitani 2011), which is similar to the pattern for talc (Mainprice et al. 2008). The antigorite examples also display similar bulk seismic properties derived from antigorite CPO regardless of the prepared sample plane (e.g., Nishii et al. 2011; Morales et al. 2018). Therefore, after filtering by the MAD values, the strongest orientation of each axis of the CPO and the resulting characteristics of the seismic anisotropy (e.g., the orientations of the strongest AVs and the fastest Vp and Vs, and the polarization directions of the fast S-waves) will not change significantly depending on the used thin-section plane (parallel or normal to the foliation) in cases of sheet silicates including talc. However, the results of grain-size analyses based on the EBSD mapping may not necessarily appear the same depending on the sample preparation plane (parallel or normal to the foliation), such as antigorite serpentinite, as demonstrated by Morales et al. (2018).

In summary, the combination of TEM and EBSD studies presented here combined with filtering of the EBSD results using MAD_{max} values (1.3–0.7°) can be used to obtain a reliable talc CPO for thin-sections made parallel to the foliation. Filtering of data using MAD values reduces mis-indexing and helps improve the accuracy of the results. This is particularly effective for poles to (001) planes. However, significant mis-indexing issues associated with 30º, 60º, and 90º rotations on the (001) plane of talc are more difficult to address. Strong concentrations of the *a*- and *b*-axes of talc can be seen on the foliation after the MAD filtering (Figs. 2(e), 3(d), and 3(e)). However, the mis-indexing issues imply the true concentrations of *a*- and *b*-axes of talc are likely to be stronger. Such uncertainties in the concentrations of *a*- and *b*-axes are unlikely to significantly affect the results regarding seismic anisotropies of talc schist, because of the similarity of the seismic properties between the *a*- and *b*-axe of talc.

4.2. Seismic anisotropy of talc schist

Talc shows different single-crystal elastic constants depending on the crystal system (triclinic or monoclinic), and the seismic anisotropy of a single talc crystal is affected by the differences between the monoclinic and triclinic structures in terms of the strength of 1) the velocity anisotropies of fast and slow shear waves (S-waves) and P-waves, 2) the polarization directions of the fast S-waves (fast direction), and 3) the delay time of the S-wave splitting defined as the time lag between Vs_1 and Vs_2 (Mainprice et al. 2008). The single grain of triclinic talc shows a larger range of S-wave velocities and can show much lower S-wave velocities than monoclinic talc: Vs_1 = 3.02–5.37 km/s and Vs_2 = 2.01–3.93 km/s for triclinic talc single crystal, and Vs_1 = 3.78–5.38 km/s and Vs_2 = 3.42–4.34 km/s for monoclinic talc single crystal at room pressure (Mainprice et al. 2008) (Figs. 7 and 8). In addition, a single grain of triclinic talc shows much stronger S-wave anisotropy than monoclinic talc: the polarization anisotropy of S-waves owing to S-wave splitting, AVs, for triclinic and monoclinic talc single crystals are ≤ ~86% and ≤ ~32% at room pressure, respectively (Mainprice et al. 2008) (Figs. 7 and 8). It is therefore suggested that the difference between the talc crystal systems strongly affects the S-wave anisotropy of talc-rich rocks (Mainprice et al. 2008) (Figs. 7 and 8). Although the difference between the anisotropies of P-waves (AVp) of triclinic and monoclinic talc single crystals is relatively small compared with AVs, the anisotropies of P-waves of talc single crystals are very strong and low Vp values can be shown depending on the seismic ray paths regardless of the crystal systems of talc (Vp = 3.94–9.13 km/s and AVp ≤ ~79% for triclinic, and Vp = 4.40–9.66 km/s and AVp ≤ ~75% for monoclinic, at room pressure) (Mainprice et al. 2008) (Figs. 7 and 8). In addition, P-waves are likely to be slower when seismic waves propagate sub-normal to the basal plane of talc, regardless of the crystal system of talc. For a tremolite single crystal, high Vp and strong AVs values are shown on the plane sub-normal to [100] of tremolite. However, the strength of the AVp and AVs of a tremolite single crystal is weaker than that for single crystals of triclinic or monoclinic talc: Vp = 6.65–7.96 km/s, AVp ≤ ~40%, Vs_1 = 4.20–4.70 km/s, Vs_2 = 4.05–4.45 km/s and AVs ≤ ~29% (Figs. 7 and 8).

We calculate the seismic anisotropies of the talc aggregate and the tremolite aggregate based on CPO patterns of talc and tremolite of Fig. 3(d) obtained by EBSD mapping in the present study in order to calculate the seismic anisotropy of talc schist as a bulk rock (Figs. 9 and 10). The effect on seismic anisotropy caused by differences in the crystal systems of talc in talc aggregates is similar to the case of a single talc crystal. Even if differences in averaging schemes for the aggregates are taken into consideration, an aggregate of triclinic talc can still show slower S-wave velocities than an aggregate of monoclinic talc: Vs_1 = 2.72–5.22 km/s and Vs_2 = 2.53–3.79 km/s for triclinic talc aggregate, and Vs_1 = 4.00–5.21 km/s and Vs_2 = 3.57–4.26 km/s for monoclinic talc aggregate at room pressure (Figs. 9 and 10). In addition, the triclinic talc aggregate shows much stronger S-wave anisotropy than the monoclinic talc aggregate: AVs for triclinic and monoclinic talc aggregates are ≤ ~47–58% and ≤ ~22–24% at room pressure, respectively (Figs. 9 and 10). AVp values of talc aggregate can be large regardless of the crystal systems of talc: Vp = 3.06–8.69 km/s and AVp ≤ ~71–83% for triclinic, and Vp = 4.25–9.39 km/s and AVp ≤ ~65–69% for monoclinic at room pressure (Figs. 9 and 10). In addition, P-waves and AVs are predicted to be faster and stronger, respectively, when seismic waves propagate sub-parallel to the foliation of the talc aggregate. In addition, in this case, the fast direction parallel to the foliation and larger delay time are also predicted. For a tremolite aggregate, high Vp and strong AVs values are predicted on the plane sub-parallel to the foliation of tremolite aggregate, as well as talc aggregate. In addition, the fast direction parallel to the foliation and larger delay time are also predicted when the seismic waves propagate sub-parallel to the foliation of the tremolite aggregate. However, the strengths of the AVp and AVs of tremolite aggregate are much weaker than those of talc aggregate: Vp = 6.48–8.19 km/s, AVp ≤ ~18%, Vs_1 = 4.11–4.81 km/s, Vs_2 = 3.95–4.57 km/s, and AVs ≤ ~13% (Figs. 9 and 10). The similarity of the relationship between the geometry of seismic ray paths and the patterns of anisotropies (including the velocities of P- and S-waves and the fast direction of S-waves due to S-wave splitting) means that the anisotropies of P- and S-waves of talc-tremolite aggregates are predicted to be weaker than talc-only aggregates and stronger than tremolite-only aggregates, and strong AVs values with the fast direction parallel to the foliation are predicted for propagation directions sub-parallel to the foliation.

To model the bulk rock of the talc-tremolite aggregate as talc schist, we used the talc and tremolite CPOs of Fig. 3 and a volume ratio for talc:tremolite of 70.9:29.1. The calculation of talc schist in the present study indicates that even if differences in averaging schemes are taken into consideration, talc schist using triclinic talc (triclinic talc schist) can also show lower Vs and stronger AVs values than talc schist using monoclinic talc (monoclinic talc schist): Vs1 = 2.95–5.09 km/s, Vs2 = 2.77–4.20 km/s, and AVs ≤ ~34–49% for triclinic talc schist, and Vs1 = 4.03–5.08 km/s, Vs2 = 3.70–4.31 km/s, and AVs ≤ ~19–20% for monoclinic talc schist at room pressure (Figs. 11 and 12). Both triclinic and monoclinic talc schists show strong AVp values: Vp = 3.41–8.51 km/s and AVp ≤ ~48–73% for triclinic talc schist, and Vp = 4.57–9.00 km/s and AVp ≤ ~48–58% for monoclinic talc schist at room pressure (Figs. 11 and 12). When the seismic waves propagate at a low angle to the plane parallel to the foliation of triclinic and monoclinic talc schists, a faster Vp, a stronger AVs, and larger delay are predicted. This means that when S-waves propagate sub-parallel to the foliation of the talc schist layer distributed parallel to the slab–mantle interface, S-wave splitting with the characteristics of trench-parallel fast direction of S-waves in the wedge mantle is predicted (Fig. 11).

Here, we compare the seismic anisotropy of talc schist with antigorite-serpentinite, which is predicted to be widely distributed in the hydrated wedge mantle of subduction zones. Lower-Vp, lower-Vs, and higher-Vp/Vs domains, as compared to dry olivine-rich domains, have been used as the indicator to find domains of highly hydrated wedge mantle in subduction zones (e.g., Nagaya et al. 2016). In addition, the detection of small differences in seismic observations of velocities (Vp and Vs) and Vp/Vs ratio within hydrated wedge mantle are thought to also be useful for finding talc-rich domains and SiO_2-rich aqueous fluid pathways within the serpentinized mantle and estimate the degree of alteration of serpentinite (Kim et al. 2013; Falcon-Suarez et al. 2017). The present study shows that S-waves that propagate normal to the foliation of talc schist can exhibit relatively low velocities, and when S-waves

This is a preprint, the final version is subject to change, of the American Mineralogist (MSA)
Cite as Authors (Year) Title. American Mineralogist, in press.
DOI: https://doi.org/10.2138/am-2020-7006

propagate parallel to the foliation of talc schist, the AVs for triclinic talc schist is approximately twice as large as that for monoclinic talc schist at room pressure (Figs. 11 and 12). However, antigorite schist shows a wide variation in Vs values (Vs_1 = 2.91–4.84 km/s and Vs_2 = 2.69–4.34 km/s at room pressure), and when S-waves propagate normal to the foliation of antigorite schist, antigorite schist can also show approximately equivalent or lower Vs than talc schist, when compared to triclinic and monoclinic talc schists, respectively (Figs. 11 and 12). Antigorite schist also shows a strong AVs when the S-waves propagate along the foliation, similar to that predicted for talc schist in the present study (Fig. 11). This figure is slightly stronger for triclinic talc schist (≤ ~34–49%) than for monoclinic talc schist (≤ ~19–20%) (Fig. 12). The AVs for antigorite schist has been given as ≤ ~32–37% in many previous experimental and natural studies (e.g., Katayama et al. 2009; Hirauchi et al. 2010; Nishii et al. 2011; Brownlee et al. 2013; Nagaya et al. 2016). The peak for antigorite schist lies between the peaks for monoclinic and triclinic talc schist given in the present study. In addition, there is a possibility that triclinic talc-rich schist may show greater S-wave anisotropy than antigorite serpentinite as demonstrated by the greater S-wave anisotropy shown by single crystals of triclinic talc (AVs ≤ ~86%, Mainprice et al. 2008) than by single antigorite single crystals (AVs for antigorite single crystal ≤ ~75%, Bezacier et al. 2010; Mainprice et al. 2015) (Figs. 7 and 8). Mis-indexing of talc orientations may also reduce the estimated seismic anisotropy, so the true value should be higher. Therefore, the S-wave anisotropy of triclinic talc schist consisting of strong CPO may be useful for finding talc-rich domains within shallow parts, such as the oceanic lithosphere compared to a deeper domain, although the CPOs and seismic anisotropies of low-temperature serpentine minerals (lizardite and chrysotile) predicted to be the dominant serpentine minerals in that domain are unclear. The Vp values and Vp/Vs ratios for S-waves that propagate normal to the foliation may also be useful to detect the presence of talc-rich domains, e.g. within fault zones in seafloor and the shallow slab–mantle interfaces in subduction zones. Although antigorite schist shows similar 3D seismic anisotropy characteristics to those of talc schist, when S-waves propagate normal to the foliation, talc schist can show significantly lower Vp values and Vp/Vs ratios than the antigorite schist at shallow parts (Figs. 11 and 12).

It is important to note that the seismic anisotropy of talc significantly decreases with increasing pressure: AVs_{max} values for talc single crystals decrease from 32% to 26% for monoclinic talc and 85% to 65% for triclinic talc as pressure increases from 0 to ~0.9 GPa (Mainprice et al. 2008) (Figs. 7 and 8). In addition, the AVs values for the talc schist in the present study changes from ≤ ~19–20% at room pressure to ≤ ~17–18% at 0.9 GPa, assuming monoclinic talc grains, and from ≤ ~34–49% at room pressure to ≤ ~30–37% at 0.9 GPa, assuming triclinic talc grains (Figs. 11 and 12). In contrast, the pressure dependence of the AVs of antigorite is weak at pressures less than ~6 GPa (Mookherjee and Capitani 2011).

The strong pressure dependence of talc seismic anisotropy means that at high P, antigorite schist can show slower S-waves and higher Vp/Vs ratios than talc schist; the range of possible AV values of antigorite schist covers the range for talc schist. Therefore, studies of seismic anisotropy are likely to be insufficient to distinguish talc-rich and antigorite-rich serpentinite regions in deeper domains of subduction zones even by careful consideration of elastic anisotropies of mineral CPOs combined with Vs and Vp/Vs and anisotropy estimates (delay time and fast direction due to S-wave splitting and Vs anisotropy) (e.g., Brownlee et al. 2013; McCormack et al. 2013; Nagaya et al. 2016).

As well as the range of Vs of talc schist, when considering the effect of the pressure, the possible range of Vp of talc schist is predicted to be smaller in a deep domain. However, Vp of talc single crystal can show much slower values than antigorite single crystal (Vp = 4.40–8.84 km/s and Vp = 4.75–9.44 km/s for triclinic and monoclinic single crystal, respectively, at 0.9 GPa, and Vp = 5.49–8.92 km/s for antigorite single crystal) (Fig. 8). In addition, as well as Vp and AVp of talc schist within the shallow domain, Vp and AVp of talc schist can also show slower and stronger values than antigorite schist at 0.9 GPa: Vp = 5.11–8.43 km/s and AVp = 37–42% for triclinic talc schist, and Vp = 5.23–8.88 km/s and AVp = 41–45% for monoclinic talc schist at 0.9 GPa, and Vp = 5.62–8.61 km/s and AVp ≤ ~33–35% for antigorite schist. Therefore, if S-waves with different ray paths through the same anisotropic domain show a larger variation in Vp values than that predicted in antigorite schist, this anisotropic domain may be composed of talc schist. In addition to these characteristics, talc-rich domains may be distinguished from antigorite-rich domains by their higher electrical resistivity, lower permeability, and higher magnetic susceptibility (Falcon-Suarez et al. 2017), although the effect of the anisotropies of talc- and antigorite schists on these properties remains unclear.

Talc-rich rocks formed by Si-metasomatism of ultramafic rocks can be widely stable from shallow domains such as ocean floor spreading centers (experimental studies (e.g., Allen and Seyfried 2003; Hirauchi et al. 2016; Oyanagi et al. 2019), the Gulf of California spreading center (Lupton 1979; Lonsdale et al. 1980), the Mid-Atlantic Ridge (Escartín et al. 2003;

Bach et al. 2004; D'Orazio et al. 2004; Boschi et al. 2006a, b), the American-Antarctic Ridge (D'Orazio et al. 2004), the Central Indian Ridge (Morishita et al. 2009), and Cerro del Almirez, Spain (the paleo-seafloor) (Marchesi et al. 2013)) to the deeper domains, such as slab-mantle interfaces in subduction zones (experimental studies (e.g., Hirauchi et al. 2013), the Catalina Schist, Santa Catalina Island, California, USA (Platt 1975; Sorensen 1988; Bebout and Barton 1989, 1993, 2002; Sorensen and Grossman 1989; Grove and Bebout 1995; King et al. 2006; Penniston-Dorland et al. 2014), Trinity thrust zone, California, USA (Peacock 1987), the Shuksan Suite, Washington, USA (Brown et al. 1982; Sorensen & Grossman 1993), Port Macquarie, Australia (Och et al. 2003), New Caledonia (Fitzherbert et al. 2004; Spandler et al. 2008), Nushima, Sanbagawa belt, Japan (Maekawa et al. 2004), Sistan Suture Zone, Iran (Fotoohi Rad et al. 2005), Cyclades, Greece (Miller et al. 2009; Marschall and Schumacher 2012; Cooperdock et al. 2018), Rio San Juan Complex, Dominican Republic (Escuder-Viruete et al. 2011; Marschall and Schumacher 2012), Livingstone Fault, New Zealand (Scott et al., 2019; Tarling et al., 2019a, 2019b), and Mariana forearc (Pabst et al. 2012)). Therefore, it is also important to clarify the minimum range of a talc-rich layer detectable by seismic observations. The measurements of the larger delay time of S-waves due to the stronger AVs values of talc and antigorite CPO may enable us to identify the distribution of hydrated mantle domains by comparing them with the predicted delay time within peridotite-rich dry mantle with B-type olivine CPO which is generally thought to be a cause of the trench-parallel fast direction in subduction zones (Faccenda et al. 2008; Kneller et al. 2008; Katayama et al. 2009; Bezacier et al. 2010; Mookherjee and Capitani 2011; Nagaya et al. 2016). Based on the present study, if we use the delay time of

DOI: https://doi.org/10.2138/am-2020-7006

S-waves to find the talc-rich layer, a talc layer with a thickness of at least ~1 to ~30 km is needed to cause a delay time of 0.1 to 1.0 s (Fig. 13). The estimated thickness of the talc-rich layer is much thinner compared to the B-type olivine-rich domain (~10–30%) (Fig. 13). However, the field studies for the metasomatic layers, including chlorite, Ca-amphiboles, and talc, derived from subduction zones have reported outcrops of talc-rich layer, mainly having a layer thickness of a few meters, and outcrops of chlorite and/or Ca-amphiboles layers that may include talc have a thickness of up to a hundred and some tens meters (e.g., Peacock and Hyndman 1999; Marschall and Schumacher 2012), as well as oceanic lithosphere (e.g., Boschi et al. 2006a). The estimation of the thickness of the talc layer in subduction zones depends on the variation of the P–T conditions, bulk rock chemistry, fluid components, and the time integrated fluid flux (e.g., Peacock and Hyndman 1999; Manning 1995, 1997). Uncertainties in fluid flux and permeabilities at high pressure are particularly large implying that obtaining reliable quantitative estimates of talc zone thicknesses from these parameters remains a challenging task. Although the exposed weak talc layer may easily disappear due to weathering, the possibility that the talc layer with a thickness on the scale of kilometers is formed at seafloors or slab-mantle interfaces in subduction zones may be low. In order to detect a talc layer with a thickness of tens to a hundred meters, very high-accuracy S-wave splitting observations that can determine the delay time on the order of ~0.001 to 0.01 s may be required. Therefore, it is difficult at present to detect and identify a talc-rich layer from S-wave splitting observations, and further improvement of the resolution of geophysical observations and resulting tomography, including the electrical resistivity, permeability, and magnetic susceptibility, is needed.

4.3. Frictional anisotropy of talc schist

In general, the friction coefficients of platy minerals including talc are controlled by the low frictional behavior on the (001) plane (e.g., Moore and Lockner 2004; Hirauchi et al. 2013; Campione and Capitani 2013; Kawai et al. 2015). Friction experiments for sheet-structured minerals suggest that single crystals have lower friction coefficients than powdered samples used as starting materials without any strong CPO patterns, because the sliding of a single crystal is accommodated along the weakest (001) plane, whereas the sliding of a powder sample of a sheet-structured mineral is more complicated and the friction coefficient of a powder sample is strongly affected by the degree of alignment of the (001) plane (e.g., Moore and Lockner 2004; Kawai et al. 2015). Therefore, the friction coefficient of talc schist with a strong CPO obtained in the present study is at most equivalent to or lower than those of powdered samples reported in experimental studies of talc. This implies that the frictional behavior of the slab-mantle interface in the wedge of the subduction zone may be significantly controlled by the low friction coefficient on the (001) plane of talc, and the predicted value of the slab-mantle interface can be lower ($\mu \leq \sim 0.05$) than that estimated from deformation experiments of talc ($\mu > \sim 0.05$) (e.g., Escartin et al. 2008; Moore and Lockner 2008; Viti 2011). The friction coefficient on the (001) plane of pyrophyllite ($Al_4Si_8O_{20}(OH)_4$)—a member of the pyrophyllite-talc group, which is a hydrous silicate with substitution of Al for Mg ions and has a similar crystal structure to talc ($Mg_3Si_4O_{10}(OH)_2$) (e.g., Rayner and Brown 1966; Kloprogge 2017)—is 0.03 (Bucholz et al. 2012), supporting our idea that talc schist with a strong CPO may have a low friction coefficient ($\mu \leq \sim 0.05$).

The formation of a CPO in talc can significantly reduce the friction coefficient of talc-bearing serpentinite. Therefore, the discussions regarding the timing and mechanism of the CPO in talc may also be important to evaluate the association with aseismic fault movement (Moore and Rymer 2007; Collettini et al. 2009) and the initiation of plate tectonics (Hirauchi et al. 2016; Karato and Barbot 2018) in addition to the coupling degree and the steady slip at the slab-mantle interface in subduction zones. However, unfortunately, in the present study, the talc CPO pattern with the *a*-axes parallel to the lineation and the *c*-axes sub-normal to the foliation is consistent both with the results of frictional experiments and the growth alignment seen in fibrous talc aggregates. In frictional experiments of sheet-structure minerals, the highly localized shear zone and the strong alignment of the (001) plane are commonly reported (e.g., Moore and Lockner 2004; Hirauchi et al. 2013; Campione and Capitani 2013; Kawai et al. 2015), and the long axes of the grains and (001) plane of deformed talc grains are generally oriented parallel to the shear direction and shear plane, respectively (Boutareaud et al. 2012). In contrast, in many cases, the long axis of talc fiber is also parallel to the *a*-axis of talc (e.g., Ball and Taylor 1962). Therefore, the timing and mechanism to develop talc CPO is unclear: growth with a preferred crystallographic orientation (e.g., epitaxial and topotaxial grain growth processes) unrelated to deformation, or related to the development of high strain zones such as the plate boundary by processes including frictional sliding, dissolution-precipitation creep and plastic deformation (e.g., Escartín et al. 2008; Viti and Collettini 2009; Collettini et al. 2009). In addition, information regarding the frictional anisotropy on the (001) plane of talc is essential to calculate the frictional property along the *a*- or *b*-axes of talc. The degree of connection of layers and patches of talc as a mechanically

DOI: https://doi.org/10.2138/am-2020-7006

weak phase in talc-bearing antigorite-serpentinite may affect the bulk rock rheology, as indicated in the examples of pargasite and phlogopite in peridotite within the upper mantle (Tommasi et al. 2017). In order to discuss the relationship with seismic events, in addition to the frictional coefficient of the talc-rich layer, it is also necessary to investigate the effective stress in talc-rich layers at various depths, the effects of other minor constituent minerals on the shear strength including the influence of the networking of mechanically weak minerals. Therefore, further investigations are necessary to facilitate more detailed discussions and clarify the implications regarding the frictional properties of talc-rich layers in subduction zones and the coupling degree at the slab–mantle interface.

5. Implications

The use of EBSD has improved our knowledge of crystal preferred orientation patterns in a wide variety of rock types and helped characterize their mechanical properties. A broad group of hydrous sheet silicates including talc and clay minerals are an important part of many fault zones and shear zones (e.g., Summers and Byerlee 1977; Wu 1978; Deng and Underwood 2001; Solum et al. 2006). Despite the potential importance of determining the anisotropy of such mechanically weak minerals, it has been difficult to determine the CPO patterns by EBSD. Recently, Nagaya et al (2017) outlined a procedure that has been successful in analyzing CPO of antigorite. Here, we expanded this approach to talc and obtained the crystal orientations of talc grains from EBSD maps for talc schist formed due to Si-metasomatism by subduction zone fluids from exotic ultramafic blocks within the Franciscan Complex from Jade Cove, and calculated the talc CPO at the slab–wedge mantle boundary (< ~450–500 ºC)

DOI: https://doi.org/10.2138/am-2020-7006

in the subduction zone. The CPO in talc schist shows that the [100] directions and the directions normal to the (001) plane of talc are strongly concentrated parallel to the lineation and normal to the foliation of the schist, respectively. The [010] directions of talc are strongly concentrated parallel to the foliation and normal to the lineation.

The combination of TEM and EBSD observations of talc grains implies that the use of EBSD orientation data of talc grains with MAD values in the range of less than 1.3º to less than 0.7º enables us to obtain a relatively accurate talc CPO when using the thin-section parallel to the foliation of talc schist. The use of the thin-section parallel to the foliation and the EBSD procedure in the present study may also enable a uniformly polished sample surface to be obtained, even for mechanically weak sheet silicates with a hardness of less than ~1–3, which results in a good indexing EBSD map and sufficient orientation data to define accurate CPOs. As with talc, CPO measurements of most clay minerals, including smectite, have not been reported. The methods used in the present study may be applicable to other mechanically-weak minerals, such as clay minerals. Smectite concentration has been found from fault zones of Tohoku-Oki (Kameda et al. 2015) and inland faults (Ohtani et al. 2000; Kuo et al. 2006). The clay minerals also develop a strong alignment, as in the case of talc, and may impart strong physical anisotropies to the fault zone. The strong anisotropy in the concentrated layer of clay minerals may also result in permeability anisotropy and affect effective stress estimations within the fault zone. The success of EBSD mapping of talc in the present study provides a base for future investigation and discussion of the existence of a region of talc along the subduction boundary, and anisotropy studies using EBSD measurements of mechanically weak minerals, such as the hydrous sheet silicates and clay minerals.

In addition, our calculation of seismic anisotropy shows that antigorite and talc schists have similar 3D seismic anisotropy characteristics. However, when S-waves propagate normal to the foliation talc schist can show significantly lower Vp values and Vp/Vs ratios than the antigorite schist at shallow parts. Therefore, in order to find talc-rich domains, the observation of Vp values and Vp/Vs ratios may be also useful by selecting the values of S-waves that propagate normal to the foliation within fault zones in the seafloor and the shallow slab–mantle interfaces in subduction zones.

It is also important to note that the seismic anisotropy of talc schist shows a greater decrease with increasing pressure compared to antigorite schist. Therefore, in deeper domains, antigorite schist can show slower S-waves and higher Vp/Vs ratios than talc schist, and AVs of antigorite schist covers the possible range of AVs values of talc schist. It is expected to be difficult to distinguish talc-rich regions in deeper domains within subduction zones from antigorite-rich serpentinite regions by seismic anisotropy modeling combined with the elastic anisotropies of mineral CPOs and seismic observations of Vs, Vp/Vs and S-wave splitting. However, Vp and AVp of talc schist can also show slower and stronger values, respectively, compared to antigorite schist at 0.9 GPa. Therefore, if S-waves with different ray paths through the same anisotropic domain show a larger variation in Vp values than that predicted in antigorite schist, this anisotropic domain may be composed of talc schist. In addition to seismic velocities and anisotropies of P- and S-waves, the combination of other geophysical observations, such as higher electrical resistivity, lower permeability, and higher magnetic susceptibility within hydrated mantle, may be effective to distinguish the talc-dominant regions from the antigorite-rich serpentinite regions, although the effect of the anisotropies of talc- and antigorite schists on these properties remains unclear and the distribution of the talc-rich layer is predicted to be limited at the slab–mantle interface (at a thickness of from a few meters to up to a hundred and some tens meters).

Acknowledgements

The authors would like to thank D. Mainprice for providing the software for analyzing the CPO data and calculating the seismic anisotropy and K. Hirauchi for providing information for the field survey. We would also like to thank N. Tsuchiya and the members of the GeoMaterial and Energy Science Group of Tohoku University and J. P. Platt, A. Lusk, W. Schmidt and T. K. Cawood for discussions, comments and encouragement. The present study was supported by Japan Society for the Promotion of Science (JSPS) Grants-in-Aid Nos. 16J01480 and 17K14405, 16H06476 and JSPS Overseas Research Fellowships to T.N. Finally, we would like to thank S. Brownlee for editorial handling and D. Moore and the anonymous reviewer for their valuable comments, which have helped to improve the manuscript.

References cited

Bach, W., Garrido, C.J., Paulick, H., Harvey, J., and Rosner, M. (2004) Seawater-peridotite interactions: First insights from ODP Leg 209, MAR 15°N. Geochemistry, Geophysics, Geosystems, 5, Q09F26, doi:10.1029/2004GC000744.

Bachmann, F., Hielscher, R., and Schaeban, H. (2011) Grain detection from 2d and 3d EBSD data-Specification of the MTEX algorithm. Ultramicroscopy, 111, 1720–1733.

Ball, M.C., and Taylor, H.F.W. (1962) The dehydration of chrysotile in air and under hydrothermal conditions. Mineralogical Magazine, 33, 467–482.

Bebout, G.E., and Barton, M.D. (1989) Fluid flow and metasomatism in a subduction zone hydrothermal system: Catalina Schist terrane, California. Geology, 17, 976–980.

Bebout, G.E., and Barton, M.D. (1993) Metasomatism during subduction: products and possible paths in the Catalina Schist, California. Chemical geology, 108, 61–92.

Bebout, G.E., and Barton, M.D. (2002) Tectonic and metasomatic mixing in a high-T, subduction-zone mélange—insights into the geochemical evolution of the slab–mantle interface. Chemical geology, 187, 79–106.

Bebout, G.E., and Penniston-Dorland, S.C. (2016) Fluid and mass transfer at subduction interfaces—The field metamorphic record. Lithos, 240–243, 228–258.

Bezacier, L., Reynard, B., Bass, J.D., Sanchez-Valle, C., and Van de Moortèle, B. (2010) Elasticity of antigorite, seismic detection of serpentinites, and anisotropy in subduction zones. Earth and Planetary Science Letters, 289, 198–208.

Boutareaud, S., Hirose, T., Andréani, M., Pec, M., Calugaru, D.-G., Boullier, A.-M., and Doan, M.-L. (2012) On the role of phyllosilicates on fault lubrication: Insight from micro- and nanostructural investigations on talc friction experiments. Journal of Geophtsical Research, 117, B08408, doi:10.1029/2011JB009006.

Bose, K., and Ganguly, J. (1995) Experimental and theoretical studies of the stability of talc, antigorite and phase A at high pressures with applications to subduction processes. Earth and Planetary Science Letters, 136, 109–121.

Boschi, C., Früh-Green, G.L., and Escartín, J. (2006a) Occurrence and significance of serpentinite-hosted, talc- and amphibole-rich fault rocks in modern oceanic settings and ophiolite complexes: An overview. Ofioliti, 31, 129–140.

Boschi, C., Früh-Green, G.L., Delacour, A. Karson, J.A., and Kelly, D.S. (2006b) Mass transfer and fluid flow during detachment faulting and development of an oceanic core complex, Atlantis Massif (MAR 30°N). Geochemistry, Geophysics, Geosystems, 7, Q01004, doi:10.1029/2005GC001074.

Bröcker, M., and Day, H.W. (1995) Low-grade blueschist facies metamorphism of metagreywackes, Franciscan Complex, Northern California. Journal of Metamorphic Geology, 13, 61–78.

Brown, E.H., Wilson, D.L., Armstrong, R.L., and Harakal, J.E. (1982) Petrologic, structural, and age relations of serpentinite, amphibolite, and blueschist in the Shuksan Suite of the Iron Mountain-Gee Point area, North Cascades, Washington. Geological Society of America Bulletin, 93, 1087–1098.

Brown, J.M., and Abramson, E.H. (2016) Elasticity of calcium and calcium-sodium amphiboles. Physics of the Earth and Planetary Interiors, 261, 161–171.

Brownlee, S.J., Hacker, B.R., Harlow, G.E., and Seward, G. (2013) Seismic signatures of a hydrated mantle wedge from antigorite crystal-preferred orientation (CPO). Earth and Planetary Science Letters, 375, 395–407.

Bucholz, E.W., Zhao, X., Sinnott, S.B., and Perry, S.S. (2012) Friction and Wear of Pyrophyllite on the Atomic Scale. Tribology Letters, 46, 159–165.

Campione, M., and Capitani, G.C. (2013) Subduction-zone earthquake complexity related to frictional anisotropy in antigorite. Nature Geoscience, 6, 847–851.

Capitani, G.C., and Stixrude, L. (2012) A first-principle investigation of antigorite up to 30 GPa: Structural behavior under compression. American Mineralogist, 97, 1177–1186.

Collettini, C., Viti, C., Smith, S.A.F., and Holdsworth, R.E. (2009) Development of interconnected talc networks and weakening of continental low-angle normal faults. Geology, 37, 567–570.

Cooper, F.J., Platt, J.P., and Anczkiewicz, R. (2011) Constraints on early Franciscan subduction rates from 2-D thermal modeling. Earth and Planetary Science Letters, 312, 69–79.

Cooperdock, E.H.G., Raia, N.H., Barnes, J.D., Stockli, D.F., and Schwarzenbach, E.M. (2018) Tectonic origin of serpentinites on Syros, Greece: Geochemical signatures of abyssal origin preserved in a HP/LT subduction complex. Lithos, 296–299, 352–364.

Deng, X., and Underwood, M.B. (2001) Abundance of smectite and the location of a plate-boundary fault, Barbados accretionary prism. Geological Society of America Bulletin, 113, 495–507.

D'Orazio, M., Boschi, C., and Brunelli, D. (2004) Talc-rich hydrothermal rocks from the St. Paul and Conrad fracture zones in the Atlantic Ocean. European Journal of Mineralogy, 16, 73–83.

Escartín, J., Mével, C., Macleod, C.J., and McCraig, A.M. (2003) Constraints on deformation conditions and the origin of oceanic detachments, The mid-atlantic ridge core complex at 15°45'N. Geochemistry, Geophysics, Geosystems, 4, 1067, doi:10.1029/2002GC000472.

Escartín, J., Andreani, M., Hirth, G., and Evans, B. (2008) Relationships between the microstructural evolution and the rheology of talc at elevated pressures and temperatures.

Earth and Planetary Science Letters, 268, 463–475.

Escuder-Viruete, J., Friedman, R., Castillo-Carrión, M., Jabites, J., and Pérez-Estaún, A. (2011) Origin and significance of the ophiolitic high-P mélanges in the northern Caribbean convergent margin: Insights from the geochemistry and large-scale structure of the Río San Juan metamorphic complex. Lithos, 127, 483–504.

Evans, B.W., and Yang, H. (1998) Fe-Mg order-disorder in tremolite–actinolite–ferro-actinolite at ambient and high temperature. American Mineralogist, 83, 458–475.

Faccenda, M., Burlini, L., Gerya, T.V., and Mainprice, D. (2008) Fault-induced seismic anisotropy by hydration in subducting oceanic plates. Nature, 455, 1097–1100.

Falcon-Suarez, I., Bayrakci, G., Minshull, T.A., North, L.J., Best, A.I., Rouméjon, S., and Party, I.E.S. (2017) Elastic and electrical properties and permeability of serpentinites from Atlantis Massif, Mid-Atlantic Ridge. Geophysical Journal International, 211, 708–721.

Fitzherbert, J.A., Clarke, G.L., Marmo, B., and Powell, R. (2004) The origin and P–T evolution of peridotites and serpentinites of NE New Caledonia: prograde interaction between continental margin and the mantle wedge. Journal of Metamorphic Geology, 22, 327–344.

Rad, G.R.F., Droop, G.T.R., Amini, S., and Moazzen, M. (2005) Eclogites and blueschists of the Sistan Suture Zone, eastern Iran: A comparison of P–T histories from a subduction mélange. Lithos, 84, 1–24.

Gatta, G.D., Merlini, M., Valdrè, G., Liermann, H.-P., Nénert, G., Rothkirch, A., Kahlenberg, V. and Pavese, A. (2013). On the crystal structure and compressional behavior of talc: a mineral of interest in petrology and material science. Physics and Chemistry of Minerals, 40, 145–156.

Grove, M., and Bebout, G.E. (1995) Cretaceous tectonic evolution of coastal southern California: Insights from the Catalina Schist. Tectonics, 14, 1290–1308.

Guo, X., Yoshino, T., and Katayama, I. (2011) Electrical conductivity anisotropy of deformed talc rocks and serpentinites at 3 GPa. Physics of the Earth and Planetary Interiors, 188, 69–81.

Hirauchi K., Tamura, A., Arai, S., Yamaguchi, H., and Hisada, K. (2008) Fertile abyssal peridotites within the Franciscan subduction complex, central California: Possible origin as detached remnants of oceanic fracture zones located close to a slow-spreading ridge. Lithos, 105, 319–328.

Hirauchi, K., Michibayashi, K., Ueda, H., and Katayama, I. (2010) Spatial variations in antigorite fabric across a serpentinite subduction channel: insights from the Ohmachi Seamount, Izu-Bonin frontal arc. Earth and Planetary Science Letters, 229, 196–206.

Hirauchi, K., den Hartog, S.A.M., and Spiers, C.J. (2013) Weakening of the slab–mantle wedge interface induced by metasomatic growth of talc. Geology, 41, 75–78.

Hirauchi, K., Fukushima, K., Kido, M., Muto, J., and Okamoto, A. (2016) Reaction-induced rheological weakening enables oceanic plate subduction. Nature Communications, 7:12550, doi: 10.1038/ncomms12550.

Hirauchi, K., Yamamoto, Y., den Hartog, S.A.M., and Niemeijer, A.R. (2019) The role of metasomatic alteration on frictional properties of subduction thrusts: An example from a serpentinite body in the Franciscan Complex, California. Earth and Planetary Science Letters, accepted.

Inoue, S., and Kogure, T. (2012) Electron backscatter diffraction (EBSD) analyses of phyllosilicates in petrographic thin-sections. American Mineralogist, 97, 755–758. doi:10.2138/am.2012.4061.

Ji, S., Li, A., Wang, Q., Long, C., Wang, H., Marcotte, D., and Salisbury, M. (2013) Seismic velocities, anisotropy, and shear-wave splitting of antigorite serpentinites and tectonic implications for subduction zones. Journal of Geophysical Research: Solid Earth, 118, 1015–1037.

Kameda, J., Shimizu, M., Ujiie, K., Hirose, T., Ikari, M., Mori, J., Oohashi, K., and Kimura, G. (2015). Pelagic smectite as an important factor in tsunamigenic slip along the Japan Trench. Geology, 43, 155–158.

Karato, S., and Barbot, S. (2018) Dynamics of fault motion and the origin of contrasting tectonic style between Earth and Venus. Scientific Reports, 8:11884, doi:10.1038/s41598-018-30174-6.

Katayama, I., Hirauchi, K., Michibayashi, K., and Ando, J. (2009) Trench-parallel anisotropy produced by serpentine deformation in the hydrated mantle wedge. Nature, 461, 1114–1117.

Kawai, K., Sakuma, H., Katayama, I., and Tamura, K. (2015) Frictional characteristics of single and polycrystalline muscovite and influence of fluid chemistry. Journal of Geophysical Research: Solid Earth, 120, 6209–6218, doi:10.1002/2015JB012286.

Kim, Y., Clayton, R.W., Asimow, P.D., and Jackson J.M. (2013) Generation of talc in the mantle wedge and its role in subduction dynamics in central Mexico. Earth and Planetary Science Letters, 384, 81–87.

King, R.L., Kohn, M.J., and Eiler, J.M. (2003) Constraints on the petrologic structure of the subduction zone slab-mantle interface from Franciscan Complex exotic ultramafic blocks. Geological Society of America Bulletin, 115, 1097–1109, doi: 10.1130/B25255.1.

King, R.L., Bebout, G.E., Moriguti, T., and Nakamura, E. (2006) Elemental mixing systematics and Sr–Nd isotope geochemistry of mélange formation: Obstacles to identification of fluid sources to arc volcanics. Earth and Planetary Science Letters, 246, 288–304.

Kloprogge, J.T. (2017) Chapter 6 - Raman Spectroscopy of Clay Minerals. Developments in Clay Science, 8, 150–199.

Kneller, E.A., Long, M.D., and van Keken, P.E. (2008) Olivine fabric transitions and shear wave anisotropy in the Ryukyu subduction system. Earth and Planetary Science Letters, 268, 268–282.

Kouketsu, Y., Miyake, A., Igami, Y., Taguchi, T., Kagi, H., and Enami, M. (2019) Drastic effect of shearing on graphite microtexture: attention and application to Earth science. Progress in Earth and Planetary Science, 6:23, doi:10.1186/s40645-019-0271-4.

Kuo, L.-W., Song, S.-R., Yeh, E.-C., and Chen, H.-F. (2009) Clay mineral anomalies in the fault zone of the Chelungpu Fault, Taiwan, and their implications. Geophysical Research Letters, 36, L18306, doi:10.1029/2009GL039269.

Lonsdale, P.F., Bischoff, J.L., Burns, V.M., Kastner, M., and Sweeney, R.E. (1980) A high-temperature hydrothermal deposit on the seabed at a gulf of California spreading center. Earth and Planetary Science Letters, 49, 8–20.

Lupton, J.E. (1979) Helium-3 in the Guaymas Basin: Evidence for injection of mantle volatiles in the Gulf of California. Journal of Geophysical Research, 84, 7446–7452.

Maekawa, H., Yamamoto, K., Ueno, T., Osada., Y., and Nogami, N. (2004) Significance of Serpentinites and Related Rocks in the High-Pressure Metamorphic Terranes, Circum-Pacific Regions. International Geology Review, 46, 426–444.

Mainprice, D. (1990) Fortran program to calculate seismic anisotropy from the lattice preferred orientation of minerals. Computers and Geosciences, 16, 385–393.

Mainprice, D., Page, Y.L., Rodgers, J., and Jouanna, P. (2008) Ab initio elastic properties of talc from 0 to 12 GPa: Interpretation of seismic velocities at mantle pressures and prediction of auxetic behaviour at low pressure. Earth and Planetary Science Letters, 274, 327–338.

Mainprice, D. (2015) Seismic anisotropy of the deep Earth from a mineral and rock physics perspective. In G. Schubert, Ed., Treatise on Geophysics, 2nd ed., 2, 487–539 p. Elsevier, Oxford.

Manning, C.E. (1995) Phase-equilibrium controls on SiO_2 metasomatism by aqueous fluid in subduction zones: Reaction at constant pressure and temperature. International Geology Review, 37, 1074–1093.

Manning, C.E. (1997) Coupled reaction and flow in subduction zones: Si metasomatism of the mantle wedge. In B. Jamtveit, and B.W.D. Yardley, Ed., Fluid flow and transport in rocks, p. 139–148. Chapman and Hall, London.

Marschall, H.R., and Schumacher, J.C. (2012) Arc magmas sourced from mélange diapirs in subduction zones. Nature Geoscience, 5, 862–867.

Marchesi, C., Garrido, C.J., Padrón-Navarta, J.A., Sánchez-Vizcaíno, V.L., and Gómez-

Pugnaire, M.T. (2013) Element mobility from seafloor serpentinization to high-pressure dehydration of antigorite in subducted serpentinite: Insights from the Cerro del Almirez ultramafic massif (southern Spain). Lithos, 178, 128–142.

McCormack, K., Wirth, E.A., and Long, M.D. (2013) B-type olivine fabric and mantle wedge serpentinization beneath the Ryukyu arc. Geophysical Research Letters, 40, 1–6, doi:10.1002/grl.50369.

Miller, D.P., Marschall, H.R., and Schumacher, J.C. (2009) Metasomatic formation and petrology of blueschist-facies hybrid rocks from Syros (Greece): Implications for reactions at the slab–mantle interface. Lithos, 107, 53–67.

Mookherjee, M., and Capitani., G.C. (2011) Trench parallel anisotropy and large delay times: Elasticity and anisotropy of antigorite at high pressures. Geophysical Research Letters, 38, L09315, doi:10.1029/2011GL047160.

Mookherjee, M. and Mainprice, D. (2014) Unusually large shear wave anisotropy for chlorite in subduction zone settings. Geophysical Research Letters, 41, 1506–1513.

Moore, D.E., and Lockner, D.A. (2004) Crystallographic controls on the frictional behavior of dry and water-saturated sheet structure minerals. Journal of Geophysical Research, 109, B03401, doi:10.1029/2003JB002582.

Moore, D.E., and Lockner, D.A. (2007) Comparative Deformation Behavior of Minerals in Serpentinized Ultramafic Rock: Application to the Slab-Mantle Interface in Subduction Zones. International Geology Review, 49, 401–415.

Moore, D.E., and Lockner, D.A. (2008) Talc friction in the temperature range 25º–400 ºC: Relevance for Fault-Zone Weakening. Tectonophysics, 449, 120–132.

Moore, D.E., and Rymer, M.J. (2007) Talc-bearing serpentinite and the creeping section of the San Andreas fault. Nature, 448, 795–797.

Morales, L.F.G., Mainprice, D., and Kern, H. (2018) Olivine-antigorite orientation relationships: Microstructures, phase boundary misorientations and the effect of cracks in the seismic properties of serpentinites. Tectonophysics, 724–725, 93–115.

Morishige, M., and van Keken, P.E. (2017) Along-arc variation in short-term slow slip events caused by 3-D fluid migration in subduction zones. Journal of Geophysical Research: Solid Earth, 122, 1434–1448, doi:10.1002/2016JB013091.

Morishita, T., Hara, K., Nakamura, K., Sawaguchi, T., Tamura, A., Arai, S., Okino, K., Takai, K., and Kumagai, H. (2009) Igneous, alteration and exhumation processes recorded in abyssal peridotites and related fault rocks from an oceanic core complex along the Central Indian Ridge. Journal of Petrology, 50, 1299–1325.

Nagaya, T., Wallis, S.R., Kobayashi, H., Michibayashi, K., Mizukami, T., Seto, Y., Miyake, A., and Matsumoto, M. (2014) Dehydration breakdown of antigorite and the formation of B-type olivine CPO. Earth and Planetary Science Letters, 387, 67–76.

Nagaya, T., Walker, A.M., Wookey, J., Wallis, S.R., Ishii, K., and Kendall, J-.M. (2016) Seismic evidence for flow in the hydrated mantle wedge of the Ryukyu subduction zone. Scientific Reports, 6, 29981; doi: 10.1038/srep29981.

Nagaya, Y., Wallis, S.R., Seto, Y., Miyake, A., Soda, Y., Uehara, S., and Matsumoto, M. (2017) Minimizing and quantifying mis-indexing in electron backscatter diffraction (EBSD) determinations of antigorite crystal directions. Journal of Structural Geology, 95, 127–141.

Nishii, A., Wallis, S.R., Mizukami, T., and Michibayashi, K. (2011) Subduction related antigorite CPO patterns from forearc mantle in the Sanbagawa belt, southwest Japan. Journal of Structural Geology, 33, 1436–1445.

Och, D.J., Leitch, E.C., Caprarelli, G., and Watanabe, T. (2003) Blueschist and eclogite in tectonic melange, Port Macquarie, New South Wales, Australia. Mineralogical Magazine, 67, 609–624.

Ohtani, T., Fujimoto, K., Ito, H., Tanaka, H., Tomida, N., and Higuchi, T. (2000) Fault rocks and past to recent fluid characteristics from the borehole survey of the Nojima fault ruptured in the 1995 Kobe earthquake, southwest Japan. Journal of Geophysical Research, 105, 16161–16171.

Ortega-Castro, J., Hernández-Haro, N., Timón, V., Sainz-Díaz, C.I., and Hernández-Laguna, A. (2010) High-pressure behavior of 2M1 muscovite. American Mineralogist, 95, 249–259.

Oyanagi, R., Okamoto, A., and Tsuchiya, N. (2019) Silica controls on hydration kinetics during serpentinization of olivine: Insights from hydrothermal experiments and a reactive transport model. Geochimica et Cosmochimica Acta, accepted.

Pabst, S., Zack, T., Savov, I.P., Ludwig, T., Rost, D., Tonarini, S., and Vicenzi, E.P. (2012) The fate of subducted oceanic slabs in the shallow mantle: Insights from boron isotopes and light element composition of metasomatized blueschists from the Mariana forearc. Lithos, 132–133, 162–179.

Padrón-Navarta, J.A., Tommasi, A., Garrido, C.J., and Sanchez-Vizcaíno, V.L. (2012) Plastic deformation and development of antigorite crystal preferred orientation in high-pressure serpentinites. Earth and Planetary Science Letters, 349–350, 75–86.

Padrón-Navarta, J., Tommasi, A., Garrido, C., and Mainprice, D. (2015) On topotaxy and compaction during antigorite and chlorite dehydration: an experimental and natural study. Contributions to Mineralogy and Petrology, 169, 1–20.

Penniston-Dorland, S.C. Gorman, J.K., Bebout, G.E., Piccoli, P.M., and Walker, R.J. (2014) Reaction rind formation in the Catalina Schist: Deciphering a history of mechanical mixing and metasomatic alteration. Chemical Geology, 384, 47–61.

Pera, E., Mainprice, D., and Burlini, L. (2003) Anisotropic seismic properties of the upper mantle beneath the Torre Alfina area (Northern Apennines, Central Italy). Tectonophjysics, 370, 11–30.

Perdikatsis, B., and Burzlaff, H. (1981) Strukturverfeinerung am Talk $Mg_3[(OH)_2Si_4O_{10}]$. Zeitschrift für Kristallographie, 156, 177–186.

Peacock, S.M. (1987) Serpentinization and infiltration metasomatism in the Trinity peridotite, Klamath province, northern California: implications for subduction zones. Contributions to Mineralogy and Petrology, 95, 55–70.

Peacock, S.M. (1993) Large-scale hydration of the lithosphere above subducting slabs. Chemical Geology, 108, 49–59.

Peacock, S.M., and Hyndman, R.D. (1999) Hydrous minerals in the mantle wedge and the maximum depth of subduction thrust earthquakes. Geophysical Research Letters, 26, 2517–2520.

Platt, J.P. (1975) Metamorphic and deformational processes in the Franciscan Complex, California: Some insights from the Catalina Schist terrane. Geological Society of America

Bulletin, 86, 1337–1347.

Rayner, J.H., and Brown, G. (1966) Structure of Pyrophyllite. Clays and Clay Minerals, 13, 73–84.

Schmidt, W., and Platt, J. (2019) Metamorphic temperatures and pressures across the eastern Franciscan: Implications for underplating and exhumation. Lithosphere, under reviewed.

Scott, J.M., Smith, S.A.F., Tarling, M.S., le Roux, P.J., Harris, C., Hoffmann, J.E., Scherzer, S., and Tulley, C.J. (2019) Element and Sr–O isotope redistribution across a plate boundary-scale crustal serpentinite mélange shear zone, and implications for the slab-mantle interface. Earth and Planetary Science Letters 522, 198–209.

Solum, J.G., Hickman, S.H., Lockner, D.A., Moore, D.E., van der Pluijm, B.A., Schleicher, A.M., Evans, J.P. (2006) Mineralogical characterization of protolith and fault rocks from the SAFOD Main Hole. Geophysical Research Letters, 33, L21314, doi:10.1029/2006GL027285.

Sorensen, S.S. (1988) Petrology of amphibolite-facies mafic and ultramafic rocks from the Catalina Schist, southern California: metasomatism and migmatization in a subduction zone metamorphic setting. Journal of Metamorphic Geology, 6, 405–435.

Sorensen, S.S., and Grossman, J.N. (1989) Enrichment of trace elements in garnet amphibolites from a paleo-subduction zone: Catalina Schist, southern California. Geochimica et Cosmochimica Acta, 53, 3155–3177.

Sorensen, S.S., and Grossman, J.N. (1993) Accessory minerals and subduction zone metasomatism: a geochemical comparison of two mélanges (Washington and California, U.S.A.). Chemical Geology, 110, 269–297.

Spandler, C., Hermann, J., Faure, K., Mavrogenes, J.A., and Arculus, R.J. (2008) The importance of talc and chlorite "hybrid" rocks for volatile recycling through subduction zones; evidence from the high-pressure subduction mélange of New Caledonia. Contributions to Mineralogy and Petrology, 155, 181–198.

Spear, F.S. (1995) Metamorphic phase equilibria and pressure-temperature-time paths, 799 p. Mineralogical Society of America, Washington, D.C.

Summers, R., and Byerlee, J. (1977) A note on the effect of fault gouge composition on the stability of frictional sliding. International Journal of Rock Mechanics and Mining Sciences & Geomechanics Abstracts, 14, 155–160.

Stixrude, L. (2002) Talc under tension and compression: Spinodal instability, elasticity, and structure. Journal of Geophysical Research, 107, B12, 2327, doi:10.1029/2001JB001684.

Tarling, M.S., Smith, S.A.F., and Scott, J.M. (2019a) Fluid overpressure from chemical reactions in serpentinite within the source region of deep episodic tremor. Nature Geoscience, doi:10.1038/s41561-019-0470-z.

Tarling, M.S., Smith, S.A.F., Scott, J.M., Rooney, J.S., Viti, C., and Gordon, K.C. (2019b) The internal structure and composition of a plate-boundary-scale serpentinite shear zone: the Livingstone Fault, New Zealand. Solid Earth, 10, 1025–1047.

Tommasi, A., Langone, A., Padrón-Navarta, J.A., Zanetti, A., and Vauchez, A. (2017) Hydrous melts weaken the mantle, crystallization of pargasite and phlogopite does not: Insights from a petrostructural study of the Finero peridotites, southern Alps. Earth and Planetary Science Letters, 477, 59–72.

Ulian, G., Tosoni, S., and Valdrè, G. (2012) The compressional behaviour and the mechanical properties of talc [$Mg_3Si_4O_{10}(OH)_2$]: a density functional theory investigation. Physics and Chemistry of Minerals, 41, 639–650.

Van de Moortele, B., Bezacier, L., Trullenque, G., and Reynard, B. (2010) Electron back-scattering diffraction (EBSD) measurements of antigorite lattice-preferred orientations (LPO). Journal of Microscopy, 239, 245–248.

Viti, C. (2011) Exploring fault rocks at the nanoscale. Journal of Structural Geology, 33, 1715–1727.

Viti, C., and Collettini, C. (2009) Growth and deformation mechanisms of talc along a natural fault: a micro/nanostructural investigation. Contributions to Mineralogy and Petrology, 158, 529–542.

Wakabayashi, J. (1992) Nappes, tectonics of oblique plate convergence, and metamorphic evolution related to 140 million years of continuous subduction, Franciscan Complex, California. The Journal of Geology, 100, 19–40.

Wang, Y., Panzik, J.E., Kiefer, B., and Lee, K.K.M. (2012) Crystal structure of graphite under room-temperature compression and decompression. Scientific Reports, 2, 520; doi: 10.1038/srep00520.

Watanabe, T., Shirasugi, Y., and Michibayashi, K. (2014) A new method for calculating seismic velocities in rocks containing strongly dimensionally anisotropic mineral grains and its application to antigorite-bearing serpentinite mylonites. Earth and Planetary Science Letters, 391, 24–35.

Wu, F.T. (1978) Mineralogy and physical nature of clay gouge. Pure and Applied Geophysics, 116, 655–689.

This is a preprint, the final version is subject to change, of the American Mineralogist (MSA)
Cite as Authors (Year) Title. American Mineralogist, in press.
DOI: https://doi.org/10.2138/am-2020-7006

Yoneda, A., Yonehara, M., and Osako, M. (2012) Anisotropic thermal properties of talc under high temperature and pressure. Physics of the Earth and Planetary Interiors, 190–191, 10–14.

Figure captions

Figure 1. Locality maps (a and b) of the study area on the west coast of central California, and geological map (c) of the Franciscan Complex at Jade Cove. (a) Simplified maps of California, USA, indicating the study area. (b) Coastline of central California. The area of Fig. 1(c) is shown by a dashed line. (c) Expanded view of the geological map of Jade Cove in the study area. The arrow shows the sample location. JKfm: metagraywacke mélange matrix, JKfu: tectonic inclusions of ultramafic material, Qal: quaternary cover alluvium, and Qls: landslide debris. Modified from King et al. (2003) and Hirauchi and Yamaguchi (2007).

Figure 2. EBSD mapping areas ((a) through (d)) and resulting talc CPO (e). (a) EBSD mapping area (Area 1) in the backscattered electron composition (BEC) image of talc schist from Jade Cove using a thin-section prepared parallel to the foliation. Purple points indicate indexing points of talc. X and Z are parallel to the horizontal and vertical lines of the image, respectively, and Y is normal to the XZ-plane. (b) Phase map of talc obtained by EBSD mapping of Area 1. An enlarged BEC image of the region marked by the red border is shown in Fig. 3. (c) Band contrast (BC) image of the EBSD mapping of Area 1. This image is

constructed based on the brightness of all detected Kikuchi bands. Arrows show the direction of the relationships of the image plane with L (the mineral lineation) and S (the foliation). (d) All Euler image on the BC image of Area 1. The indexing points in Figs. 1(a), 1(b), and 1(d) show data for talc orientations with MAD values of less than 2.0º. None of the Channel5 correction functions were applied. A step size of 1 μm was used. (e) Talc CPO for the range of MAD values of less than 1.3º calculated using talc orientation data obtained by EBSD mapping of Area 1. The reference frame indicated by X, Y, and Z is the same as in Fig. 2(a) and the Y-direction is normal to the foliation (N.B. this use is different from the standard use of X, Y and Z to label the principle axes of finite strain). The CPO is presented in equal-area, lower-hemisphere projections with the foliation parallel to the XZ plane. The open circles represent the direction parallel to L. Open squares represent the directions of the strongest concentrations. The contours of the color scales and associated numbers show multiples of uniform distribution (m.u.d.). N represents the number of measured points. The talc CPO is represented by three pole figures for the [100] and [010] directions and the normal to the (001) plane of talc from left to right. The figures were prepared using software of D. Mainprice (Mainprice 1990).

Figure 3. EBSD mapping area ((a) through (c)) and resulting talc CPO ((d) and (e)). (a) BEC image of the area indicated by the red border in Figs. 2(b) through 2(d). Arrows show the direction of the relationships of the image plane with L (the mineral lineation) and S (the foliation). X and Z are parallel to the horizontal and vertical lines of this image, respectively,

and Y is normal to the XZ-plane. The XZ plane is parallel to the foliation, and the Y-direction is normal to the foliation. EBSD mapping of the area enclosed by the white border (Area 2) is shown in Figs. 3(b) and 3(c). An enlarged BEC image of the area enclosed by the yellow border is shown in Fig. 4. (b) Phase map on the BC image of EBSD mapping of Area 2. Phase map of talc and tremolite obtained by EBSD mapping of Area 2. The BC image is constructed based on the brightness of all detected Kikuchi bands. (c) All Euler image on the BC image of Area 2. The talc CPO obtained EBSD measurement of the light blue square (Area 3) is shown in Fig. 3(e). For Figs. 3(b) and 3(c), none of the Channel 5 correction functions are applied, and a step size of 500 nm is used. (d) Talc and tremolite CPOs for the range of MAD values of less than 1.0º calculated using talc and orientation data obtained by EBSD mapping of Area 2. The reference frame indicated by X, Y and Z is the same as in Fig. 3(a), and the Y-direction is normal to the foliation. The open circles indicate the direction parallel to L. Open squares indicate the directions of the strongest concentrations. The talc and tremolite CPOs are represented by three pole figures for the [100] and [010] directions and the normal to the (001) plane of talc and tremolite from left to right. (e) Talc and tremolite CPOs for the range of MAD values of less than 1.0º calculated using talc and orientation data obtained by EBSD mapping of Area 3. All others features are shown in the same way as in Fig. 3(d).

Figure 4. Talc single grain used for the comparison of the EBSD results with TEM observation and EBSD results of the single grain. (a) BEC image of Area 4 in Fig. 3(a) including the talc single grain used for the comparison of EBSD results with TEM

This is a preprint, the final version is subject to change, of the American Mineralogist (MSA)
Cite as Authors (Year) Title. American Mineralogist, in press.
DOI: https://doi.org/10.2138/am-2020-7006

observation. X and Z are parallel to the horizontal and vertical lines of this image, respectively, and Y is normal to the XZ-plane. These are the same directions as in Fig. 3(a). The XZ plane is parallel to the foliation, and the Y-direction is normal to the foliation. EBSD mapping of the area enclosed by the green border (Area 5) is shown in Fig. 4(b). The dashed borders indicate the areas coated with Pt to extract sample leaves (TEM samples 1 and 2). The red dashed lines with the direction from (A) to (B) show the same direction of TEM samples in Figs. 6(a) and 6(d). (b) All Euler image of talc obtained by EBSD mapping of Areas 5 and 6 within the talc single grain. Area 6 is a detailed view of the domain surrounded by a blue border in Area 5. None of the Channel 5 correction functions are applied, and a step size of 100 nm is used. (c) Representative examples of mis-indexing orientations of talc with various MAD values within the talc single grain in EBSD measurements. Indexing points of talc in the same grain with very similar detected Kikuchi patterns (left) shows the different talc orientations shown by simulated Kikuchi patterns (right). The numbers of indexing points (talc 1, talc 2, and talc 3) correspond to those in Area 6 in Fig. 4(b). Each point has a pixel size of 0.1 μm × 0.1 μm. For each measured point, the raw Kikuchi pattern is shown on the left, and the Kikuchi pattern with the simulated pattern is shown on the right. (d) Dot plots of crystallographic orientations of indexing points (talc 1, talc 2, and talc 3) on the pole figures. The yellowish-brown squares indicate the directions of the crystallographic orientations of talc 1, talc 2, and talc 3 obtained by EBSD. The reference frame shown by X, Y, and Z is the same as in Figs. 3(a) and 4(a). The XZ plane is parallel to the foliation, and the Y-direction is normal to the foliation. All other features are shown in the same way as in Fig. 2(e).

Figure 5. Pole figure of crystallographic orientations of the talc single grain obtained from EBSD mapping of Area 5 in Fig. 4 for different maximum upper MAD values and from TEM measurements. The concentration of each direction is expressed using contours (left) and dot plots (right). The yellowish-brown squares indicate the directions of the strongest concentrations in the EBSD measurements. The orientations measured by TEM are shown by the red and purple squares for TEM samples 1 and 2, respectively, on the pole figures. The open circles represent the direction parallel to L. All other features are shown in the same way as in Fig. 4(d).

Figure 6. TEM images of the talc single crystals (TEM samples 1 and 2) shown in Fig. 4(a). Bright field TEM images of TEM sample 1 (a) and TEM sample 2 (b) (domains surrounded by red dashed borders in Fig. 4a). The red thick dashed lines with the direction from (A) to (B) indicate the same direction as in Fig. 4(a). The reference frame shown by X, Y, and Z is the same as in Figs. 3(a) and 4(a). The XZ plane is parallel to the foliation, and the Y-direction is normal to the foliation. (c) Detailed view of the domain surrounded by a brown border in Fig. 6(a). TEM sample 1 is rotated -1.2º and 10.8º around the X- and Y-directions, respectively. The positive directions of the rotations around the X- and Y-directions are shown in Fig. 6(a). The pink domains show the location of the electron diffraction pattern domain shown in Fig. 6(c). (d) Detailed view of the domain surrounded by a brown border in Fig. 6(b). TEM sample 2 is rotated -5.4º and 11.5º around the Z- and Y-

DOI: https://doi.org/10.2138/am-2020-7006

directions, respectively. The positive directions of the rotations around the X- and Y-directions are shown in Fig. 6(b). The pink domains show the locations of the electron diffraction pattern domains shown in Fig. 6(f). (e) Electron diffraction pattern along the [100] direction, where the sample in Fig. 10(a) is rotated -1.2º and 10.8º around the X- and Y-directions, respectively. (f) Electron diffraction pattern along the [010] direction, where the sample in Fig. 10(b) is rotated -5.4º and 11.5º around the Z- and Y-directions, respectively.

Figure 7. Seismic anisotropy corresponding to single crystals of (a) talc, (b) tremolite, and (c) antigorite. The calculations were performed assuming the different pressure conditions of room pressure (0 GPa) and 0.9 GPa and crystal systems of talc of monoclinic and triclinic polytypes. The elastic constants of talc, tremolite and antigorite are calculated following Mainprice et al. (2008), Brown and Abramson (2016) and Bezacier et al. (2010). The plots are all lower-hemisphere equal-area. The contours show multiples of uniform density. Black and white squares represent the maximum and minimum for each figure, and color shading of each figure is also shown on the right. In the figure of Vs_1 Polarization, each small segment on the figure represents the trace of the polarization plane on the point at which a fast S-wave penetrates the hemisphere.

Figure 8. Ranges of velocities (km/s) and anisotropies (%) of P- and S-waves and Poisson’s ratios (Vp/Vs) based on the seismic anisotropies of talc, tremolite, and

DOI: https://doi.org/10.2138/am-2020-7006

antigorite single crystals of Fig. 7. The colored numbers in the figures correspond to the numbers of the same color in the lower right legend. The colors of the horizontal bar in the figures correspond to the same colors in the lower right legend. The colored horizontal bars indicate the range of values, and black vertical bars indicate the lowest and highest values of Fig. 7.

Figure 9. Seismic anisotropies corresponding to (a) the talc aggregate and (b) the tremolite aggregate calculated from CPO patterns of talc and tremolite from the talc schist, Jade Cove. The calculations were performed assuming the Voigt-Reuss-Hill average scheme for talc aggregate and tremolite aggregate. Plots are oriented such that the foliation is horizontal and the lineation is east–west. All other features are shown in the same way as in Fig. 7.

Figure 10. Ranges of velocities (km/s) and anisotropies (%) of P- and S-waves and Poisson's ratios (Vp/Vs) based on the seismic anisotropies of talc_aggregate and tremolite aggregate of Fig. 9. The colored horizontal bars indicate the range of values, and the black vertical bars indicate the lowest and highest values of Fig. 9, assuming the Voigt-Reuss-Hill average scheme. The gray dashed bars indicate the range of values, and gray bars show the lowest and highest values calculated assuming the Reuss and Voigt average schemes.

DOI: https://doi.org/10.2138/am-2020-7006

Abbreviations: R = Reuss average, V = Voigt average, VRH = Voigt-Reuss-Hill average. All other features are shown in the same way as in Fig. 8.

Figure 11. Seismic anisotropies corresponding to the fabric of (a) the talc schist obtained from Jade Cove in the present study and (b) antigorite schist obtained from Nagaya et al. (2014). All other features are shown in the same way as in Fig. 9.

Figure 12. Ranges of velocities (km/s) and anisotropies (%) of P- and S-waves and Poisson's ratios (Vp/Vs) based on the seismic anisotropies of the talc and antigorite schists of Fig. 11. The colored horizontal bars indicate the range of values, and the black vertical bars indicate the lowest and highest values of Fig. 11, assuming the Voigt-Reuss-Hill average scheme. The gray dashed bars indicate the range of values, and the gray bars show the lowest and highest values calculated assuming the Reuss and Voigt average schemes. All other features are shown in the same way as in Fig. 10.

Figure 13. Relationship of the delay time due to S-wave splitting and the thickness of the schist layer, estimated when seismic waves propagate parallel to the foliation and lineation of talc schist and antigorite schist. The equation between the travel distance of the shear wave within the anisotropic layer (L in kilometers) and the delay time (dt in

seconds) is L = 100 dt <Vs>/AVs, where <Vs> (km/s) is the average velocity of the Vs_1 (km/s) and Vs_2 (km/s) (e.g., Pera et al. 2003). Vs_1, Vs_2 and AVs are derived from the seismic anisotropies of the talc schists of Fig. 11(a), the antigorite schists of Fig. 11(b), and the peridotite showing B-type olivine CPO reported by Nagaya et al. (2014).

Figure 1

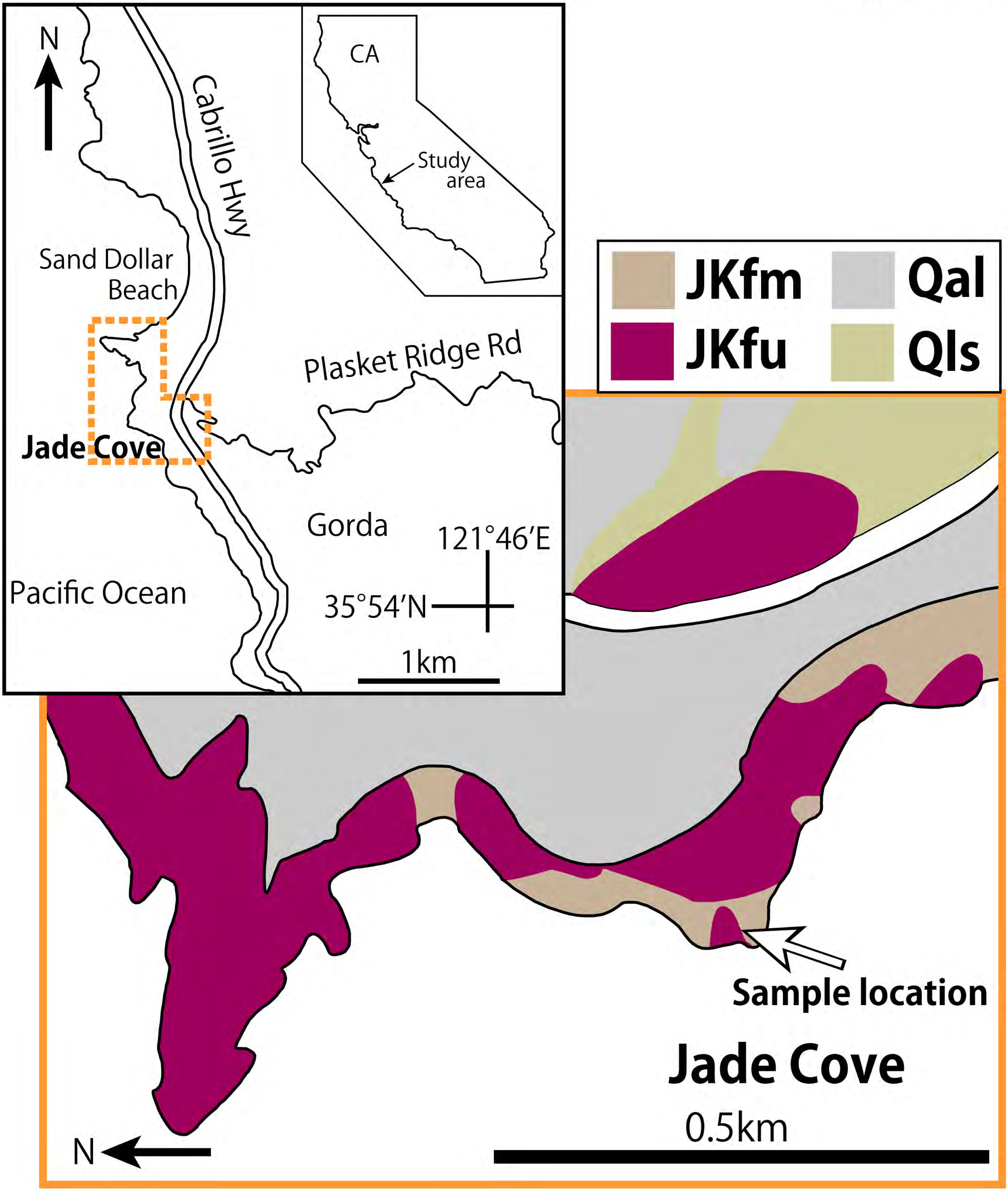
N
Cabrillo Hwy
CA
Study area
Sand Dollar Beach
Plasket Ridge Rd
Jade Cove
Gorda
121°46′E
Pacific Ocean
35°54′N
1km
JKfm
Qal
JKfu
Qls
Sample location
Jade Cove
0.5km
N

Figure 2

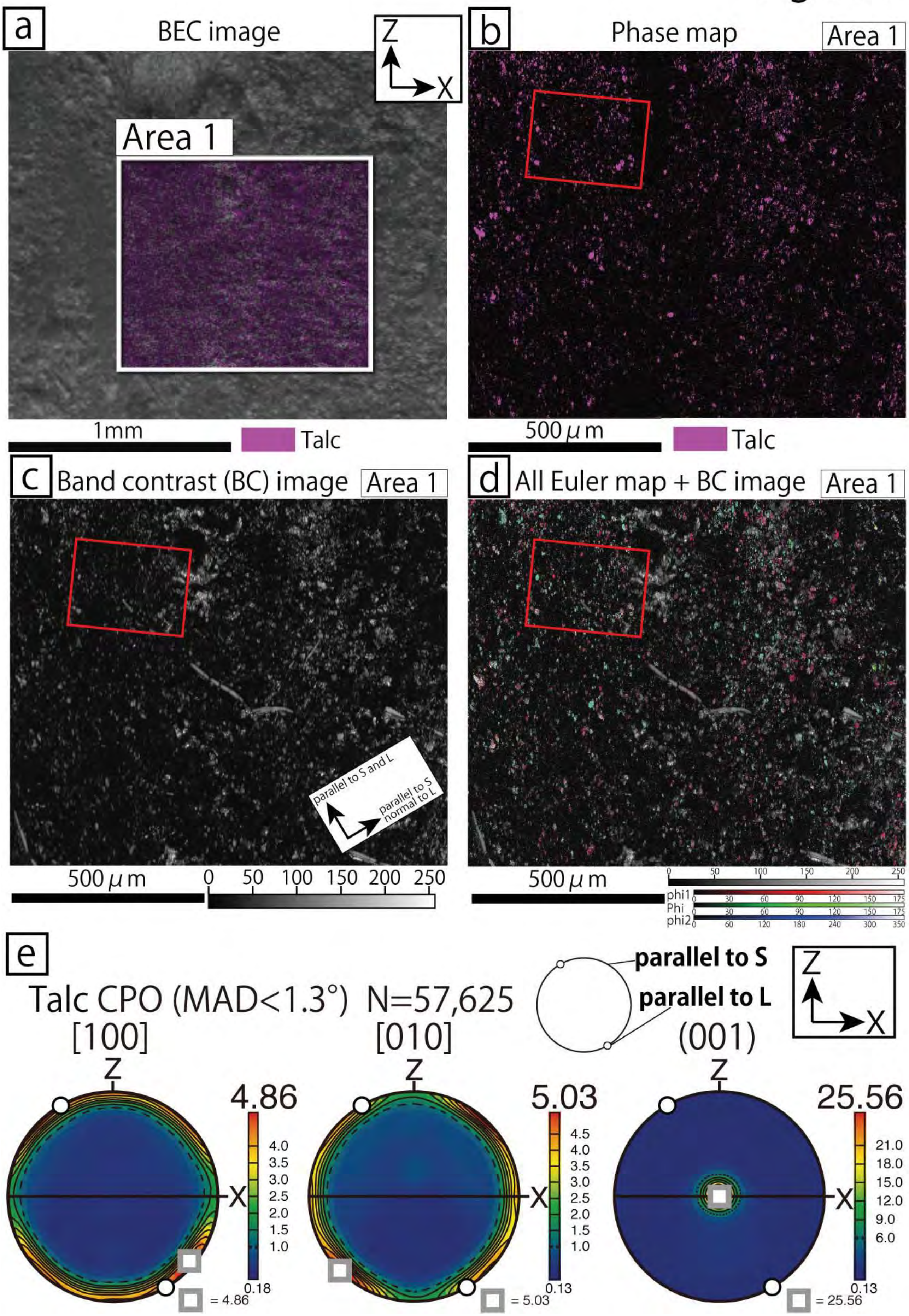

a
BEC image
Z
X
Area 1
1mm
Talc
b
Phase map
Area 1
500 μm
Talc
c
Band contrast (BC) image
Area 1
parallel to S and L
parallel to S normal to L
500 μm
0 50 100 150 200 250
d
All Euler map + BC image
Area 1
500 μm
phi1
Phi
phi2
e
Talc CPO (MAD<1.3°) N=57,625
parallel to S
parallel to L
[100]
[010]
(001)
Z
X
4.86
= 4.86
5.03
= 5.03
25.56
= 25.56

Figure 3

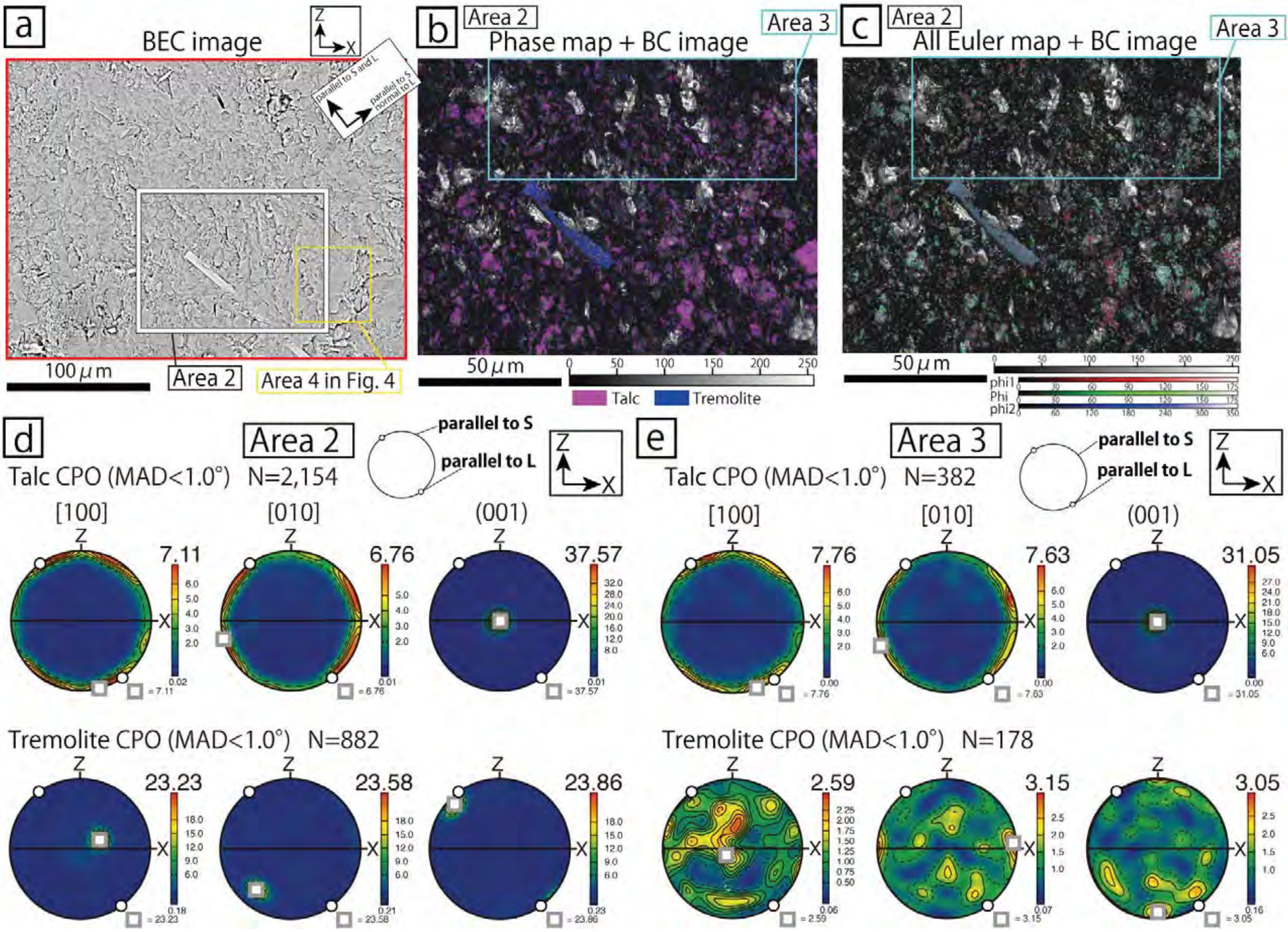

a
BEC image
parallel to S and L
parallel to S normal to L
100 μm
Area 2
Area 4 in Fig. 4
b
Area 2
Phase map + BC image
Area 3
50 μm
Talc
Tremolite
c
Area 2
All Euler map + BC image
Area 3
50 μm
phi1
Phi
phi2
d
Area 2
Talc CPO (MAD<1.0°) N=2,154
parallel to S
parallel to L
[100]
[010]
(001)
7.11
6.76
37.57
Tremolite CPO (MAD<1.0°) N=882
23.23
23.58
23.86
e
Area 3
Talc CPO (MAD<1.0°) N=382
parallel to S
parallel to L
[100]
[010]
(001)
7.76
7.63
31.05
Tremolite CPO (MAD<1.0°) N=178
2.59
3.15
3.05

Figure 4

a
Area 4
BEC image
Z
X
(A)
(B)
(A)
(B)
10 μm
Area 5
TEM sample 1
TEM sample 2
b
Area 5
All Euler map
talc 3
Area 6
talc 2
talc 1
2 μm
Area 6
phi1
Phi
phi2
0 30 60 90 120 150 175
0 30 60 90 120 150 175
0 60 120 180 240 300 350
c
talc 1 (MAD=1.75°)
talc 2 (MAD=1.55°)
talc 3 (MAD=0.91°)
d
[100]
[010]
(001)
talc 1 (MAD=1.75°)
talc 2 (MAD=1.55°)
talc 3 (MAD=0.91°)

Figure 5

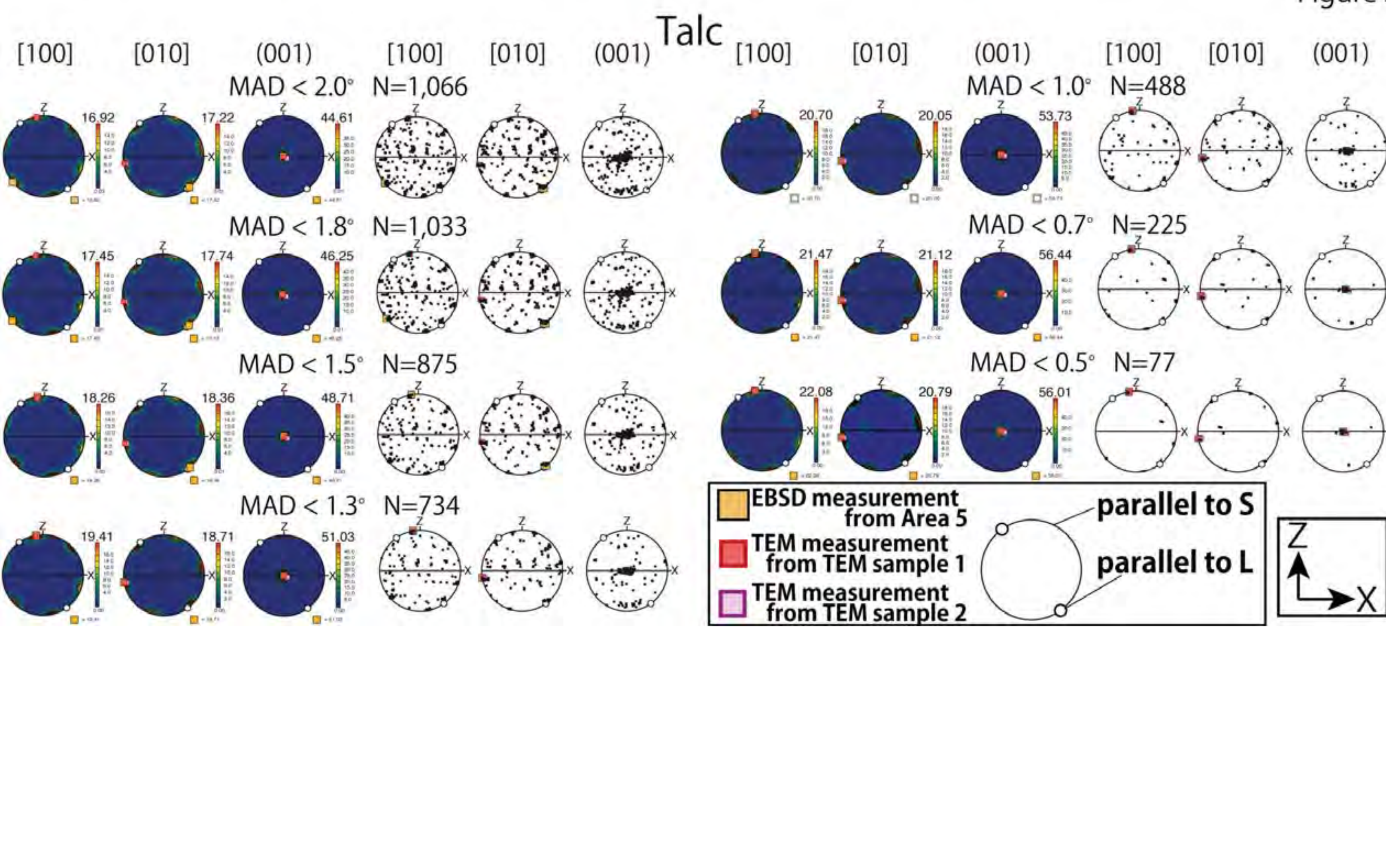

Talc
[100]
[010]
(001)
MAD < 2.0° N=1,066
MAD < 1.8° N=1,033
MAD < 1.5° N=875
MAD < 1.3° N=734
MAD < 1.0° N=488
MAD < 0.7° N=225
MAD < 0.5° N=77
EBSD measurement from Area 5
TEM measurement from TEM sample 1
TEM measurement from TEM sample 2
parallel to S
parallel to L
Z
X

Figure 6

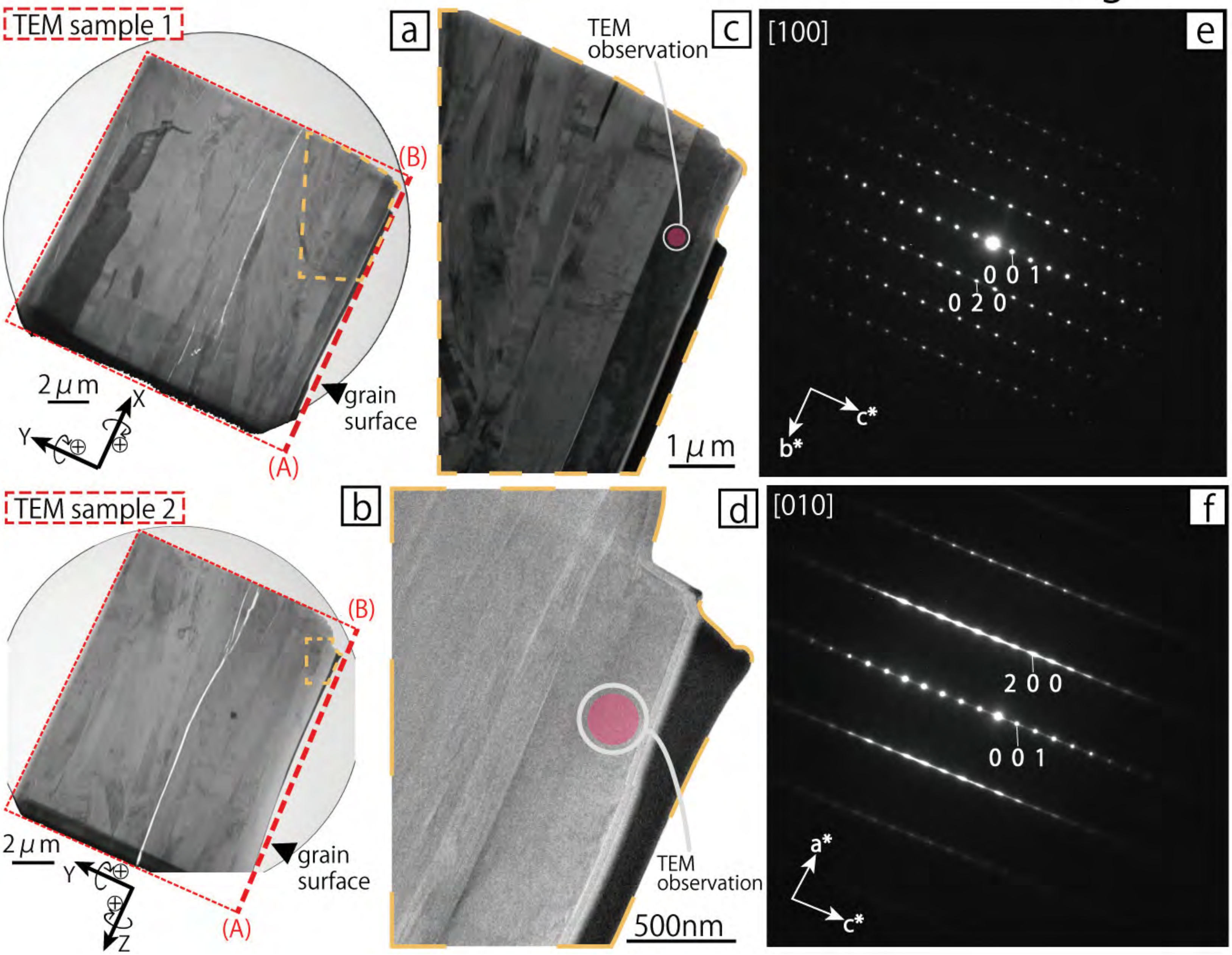

TEM sample 1
a
(B)
2 μm
X
Y
grain
surface
(A)
TEM
observation
c
1 μm
[100]
e
0 0 1
0 2 0
c*
b*
TEM sample 2
b
(B)
2 μm
Y
Z
grain
surface
(A)
d
TEM
observation
500nm
[010]
f
2 0 0
0 0 1
a*
c*

Figure 7

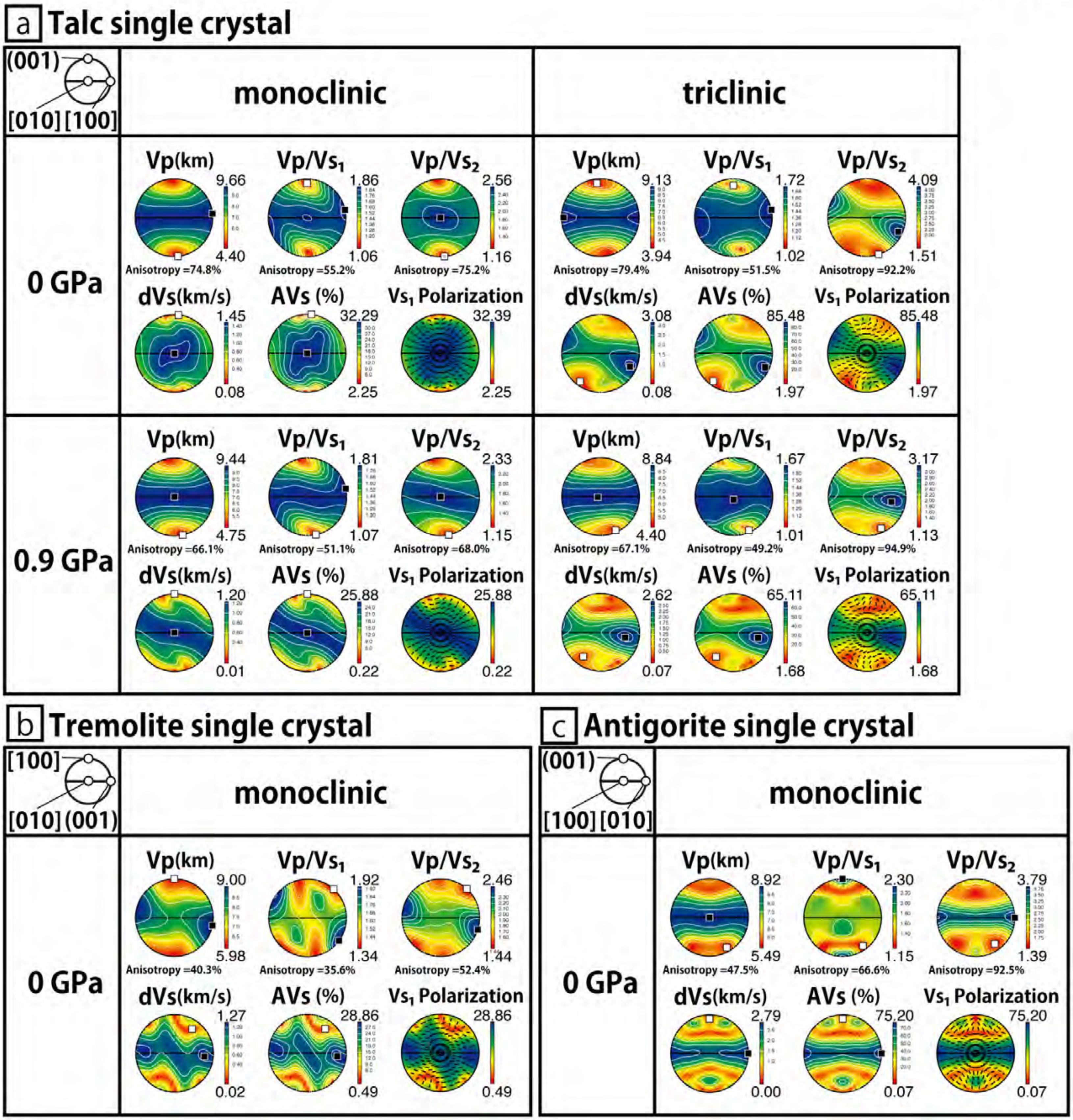

a Talc single crystal
(001)
[010] [100]
monoclinic
triclinic
0 GPa
Vp(km)
9.66
4.40
Anisotropy =74.8%
Vp/Vs1
1.86
1.06
Anisotropy =55.2%
Vp/Vs2
2.56
1.16
Anisotropy =75.2%
dVs(km/s)
1.45
0.08
AVs (%)
32.29
2.25
Vs1 Polarization
32.39
2.25
Vp(km)
9.13
3.94
Anisotropy =79.4%
Vp/Vs1
1.72
1.02
Anisotropy =51.5%
Vp/Vs2
4.09
1.51
Anisotropy =92.2%
dVs(km/s)
3.08
0.08
AVs (%)
85.48
1.97
Vs1 Polarization
85.48
1.97
0.9 GPa
Vp(km)
9.44
4.75
Anisotropy =66.1%
Vp/Vs1
1.81
1.07
Anisotropy =51.1%
Vp/Vs2
2.33
1.15
Anisotropy =68.0%
dVs(km/s)
1.20
0.01
AVs (%)
25.88
0.22
Vs1 Polarization
25.88
0.22
Vp(km)
8.84
4.40
Anisotropy =67.1%
Vp/Vs1
1.67
1.01
Anisotropy =49.2%
Vp/Vs2
3.17
1.13
Anisotropy =94.9%
dVs(km/s)
2.62
0.07
AVs (%)
65.11
1.68
Vs1 Polarization
65.11
1.68
b Tremolite single crystal
[100]
[010] (001)
monoclinic
0 GPa
Vp(km)
9.00
5.98
Anisotropy =40.3%
Vp/Vs1
1.92
1.34
Anisotropy =35.6%
Vp/Vs2
2.46
1.44
Anisotropy =52.4%
dVs(km/s)
1.27
0.02
AVs (%)
28.86
0.49
Vs1 Polarization
28.86
0.49
c Antigorite single crystal
(001)
[100] [010]
monoclinic
0 GPa
Vp(km)
8.92
5.49
Anisotropy =47.5%
Vp/Vs1
2.30
1.15
Anisotropy =66.6%
Vp/Vs2
3.79
1.39
Anisotropy =92.5%
dVs(km/s)
2.79
0.00
AVs (%)
75.20
0.07
Vs1 Polarization
75.20
0.07

Figure 8

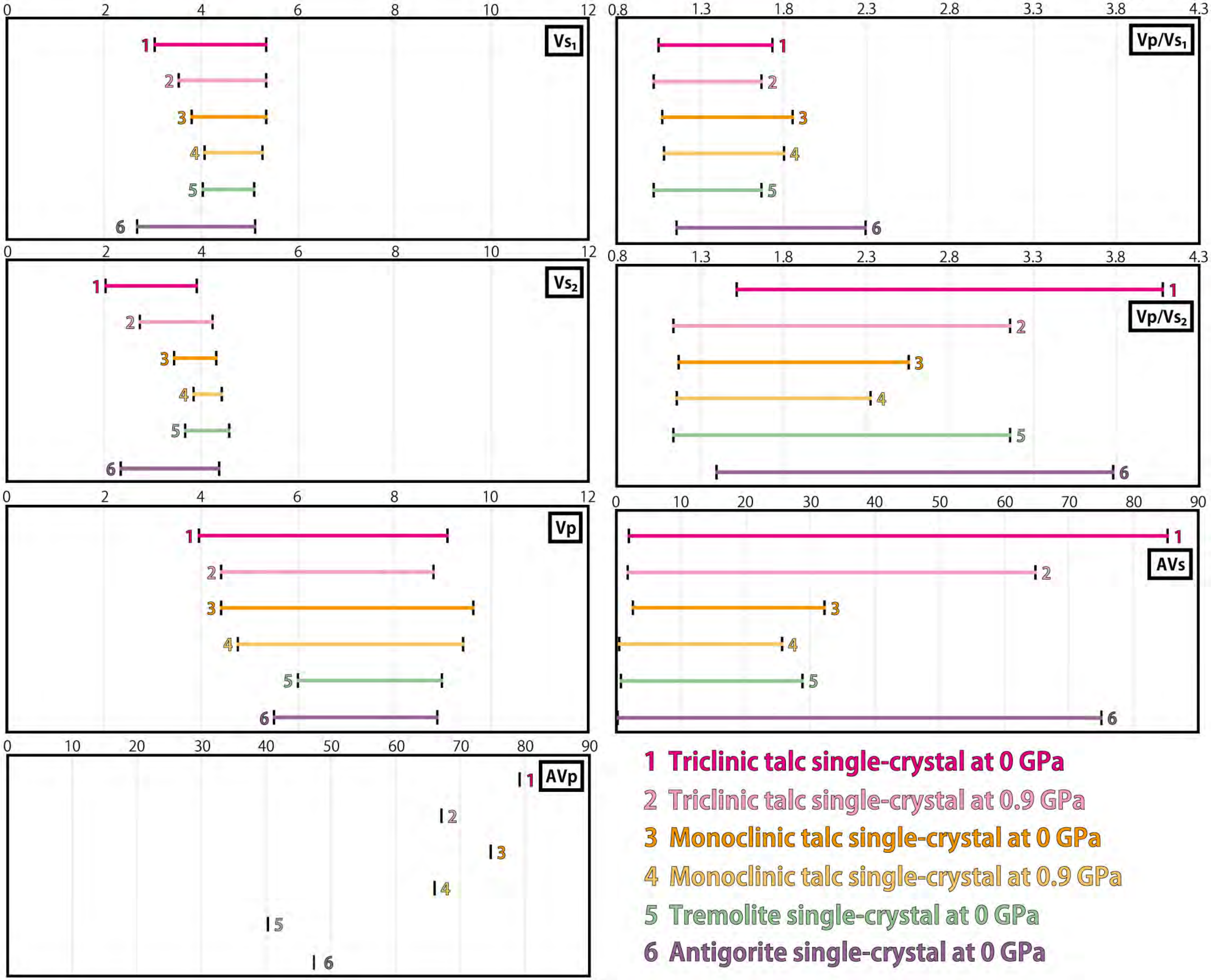
Vs1
Vp/Vs1
Vs2
Vp/Vs2
Vp
AVs
AVp
1 Triclinic talc single-crystal at 0 GPa
2 Triclinic talc single-crystal at 0.9 GPa
3 Monoclinic talc single-crystal at 0 GPa
4 Monoclinic talc single-crystal at 0.9 GPa
5 Tremolite single-crystal at 0 GPa
6 Antigorite single-crystal at 0 GPa

Figure 9

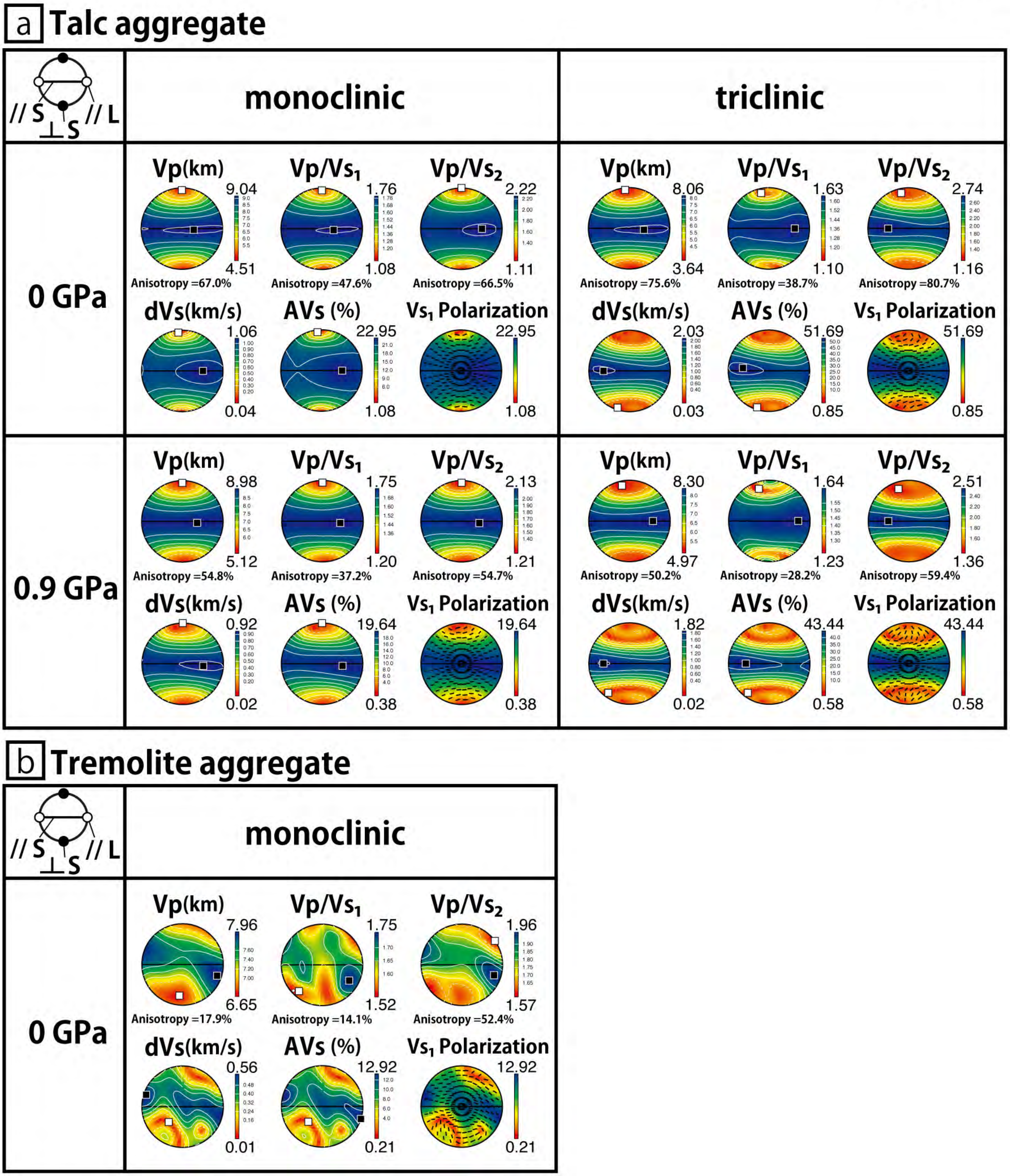

a Talc aggregate
// S
⊥S
// L
monoclinic
triclinic
0 GPa
Vp(km)
9.04
4.51
Anisotropy =67.0%
Vp/Vs1
1.76
1.08
Anisotropy =47.6%
Vp/Vs2
2.22
1.11
Anisotropy =66.5%
Vp(km)
8.06
3.64
Anisotropy =75.6%
Vp/Vs1
1.63
1.10
Anisotropy =38.7%
Vp/Vs2
2.74
1.16
Anisotropy =80.7%
dVs(km/s)
1.06
0.04
AVs (%)
22.95
1.08
Vs1 Polarization
22.95
1.08
dVs(km/s)
2.03
0.03
AVs (%)
51.69
0.85
Vs1 Polarization
51.69
0.85
0.9 GPa
Vp(km)
8.98
5.12
Anisotropy =54.8%
Vp/Vs1
1.75
1.20
Anisotropy =37.2%
Vp/Vs2
2.13
1.21
Anisotropy =54.7%
Vp(km)
8.30
4.97
Anisotropy =50.2%
Vp/Vs1
1.64
1.23
Anisotropy =28.2%
Vp/Vs2
2.51
1.36
Anisotropy =59.4%
dVs(km/s)
0.92
0.02
AVs (%)
19.64
0.38
Vs1 Polarization
19.64
0.38
dVs(km/s)
1.82
0.02
AVs (%)
43.44
0.58
Vs1 Polarization
43.44
0.58
b Tremolite aggregate
// S
⊥S
// L
monoclinic
0 GPa
Vp(km)
7.96
6.65
Anisotropy =17.9%
Vp/Vs1
1.75
1.52
Anisotropy =14.1%
Vp/Vs2
1.96
1.57
Anisotropy =52.4%
dVs(km/s)
0.56
0.01
AVs (%)
12.92
0.21
Vs1 Polarization
12.92
0.21

Figure 10

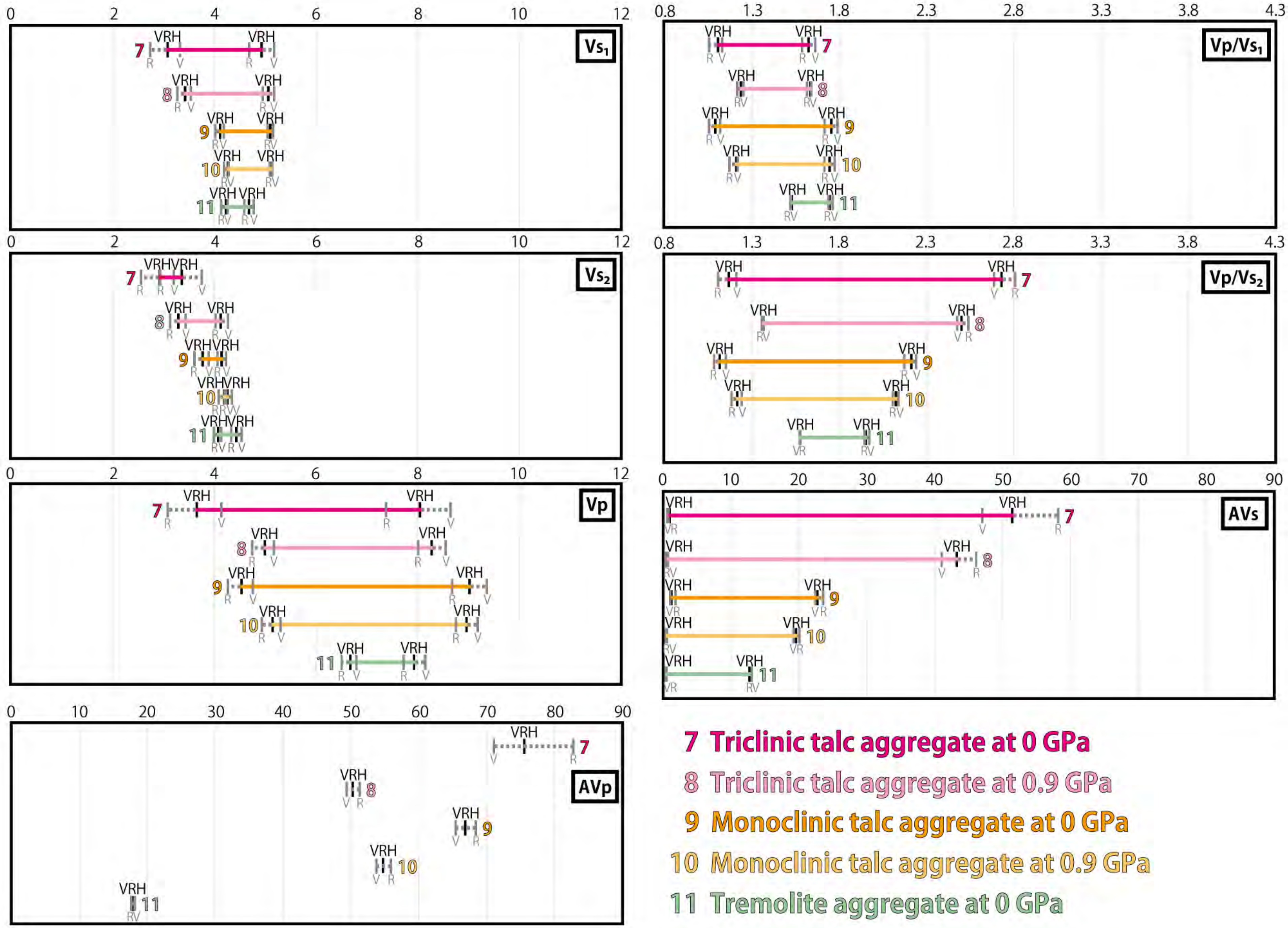

Vs1
Vp/Vs1
Vs2
Vp/Vs2
Vp
AVs
AVp
VRH
7 Triclinic talc aggregate at 0 GPa
8 Triclinic talc aggregate at 0.9 GPa
9 Monoclinic talc aggregate at 0 GPa
10 Monoclinic talc aggregate at 0.9 GPa
11 Tremolite aggregate at 0 GPa

Figure 11

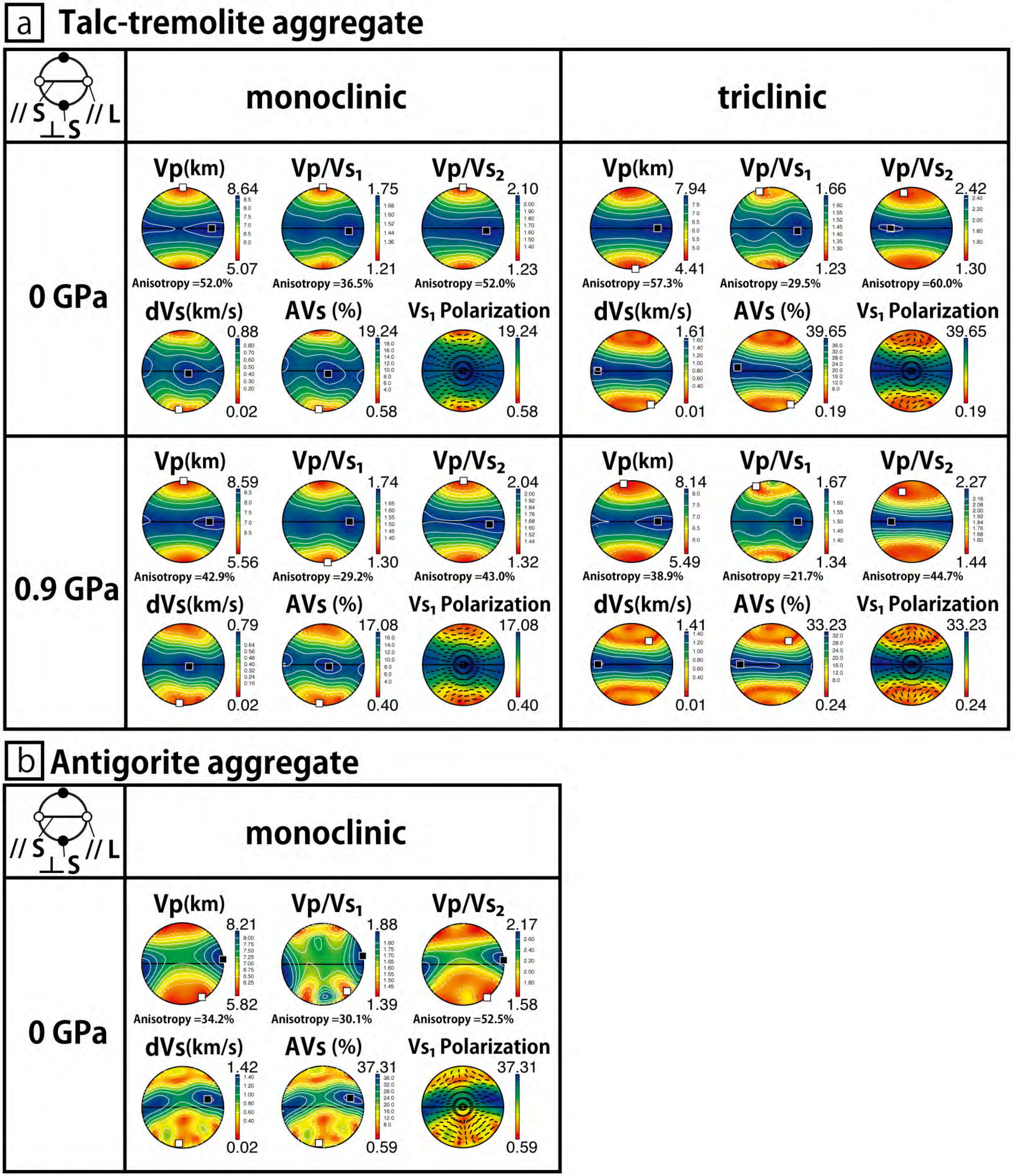
a Talc-tremolite aggregate
// S
⊥S
// L
monoclinic
triclinic
0 GPa
Vp(km)
8.64
5.07
Anisotropy =52.0%
Vp/Vs1
1.75
1.21
Anisotropy =36.5%
Vp/Vs2
2.10
1.23
Anisotropy =52.0%
dVs(km/s)
0.88
0.02
AVs (%)
19.24
0.58
Vs1 Polarization
19.24
0.58
Vp(km)
7.94
4.41
Anisotropy =57.3%
Vp/Vs1
1.66
1.23
Anisotropy =29.5%
Vp/Vs2
2.42
1.30
Anisotropy =60.0%
dVs(km/s)
1.61
0.01
AVs (%)
39.65
0.19
Vs1 Polarization
39.65
0.19
0.9 GPa
Vp(km)
8.59
5.56
Anisotropy =42.9%
Vp/Vs1
1.74
1.30
Anisotropy =29.2%
Vp/Vs2
2.04
1.32
Anisotropy =43.0%
dVs(km/s)
0.79
0.02
AVs (%)
17.08
0.40
Vs1 Polarization
17.08
0.40
Vp(km)
8.14
5.49
Anisotropy =38.9%
Vp/Vs1
1.67
1.34
Anisotropy =21.7%
Vp/Vs2
2.27
1.44
Anisotropy =44.7%
dVs(km/s)
1.41
0.01
AVs (%)
33.23
0.24
Vs1 Polarization
33.23
0.24
b Antigorite aggregate
// S
⊥S
// L
monoclinic
0 GPa
Vp(km)
8.21
5.82
Anisotropy =34.2%
Vp/Vs1
1.88
1.39
Anisotropy =30.1%
Vp/Vs2
2.17
1.58
Anisotropy =52.5%
dVs(km/s)
1.42
0.02
AVs (%)
37.31
0.59
Vs1 Polarization
37.31
0.59

Figure 12

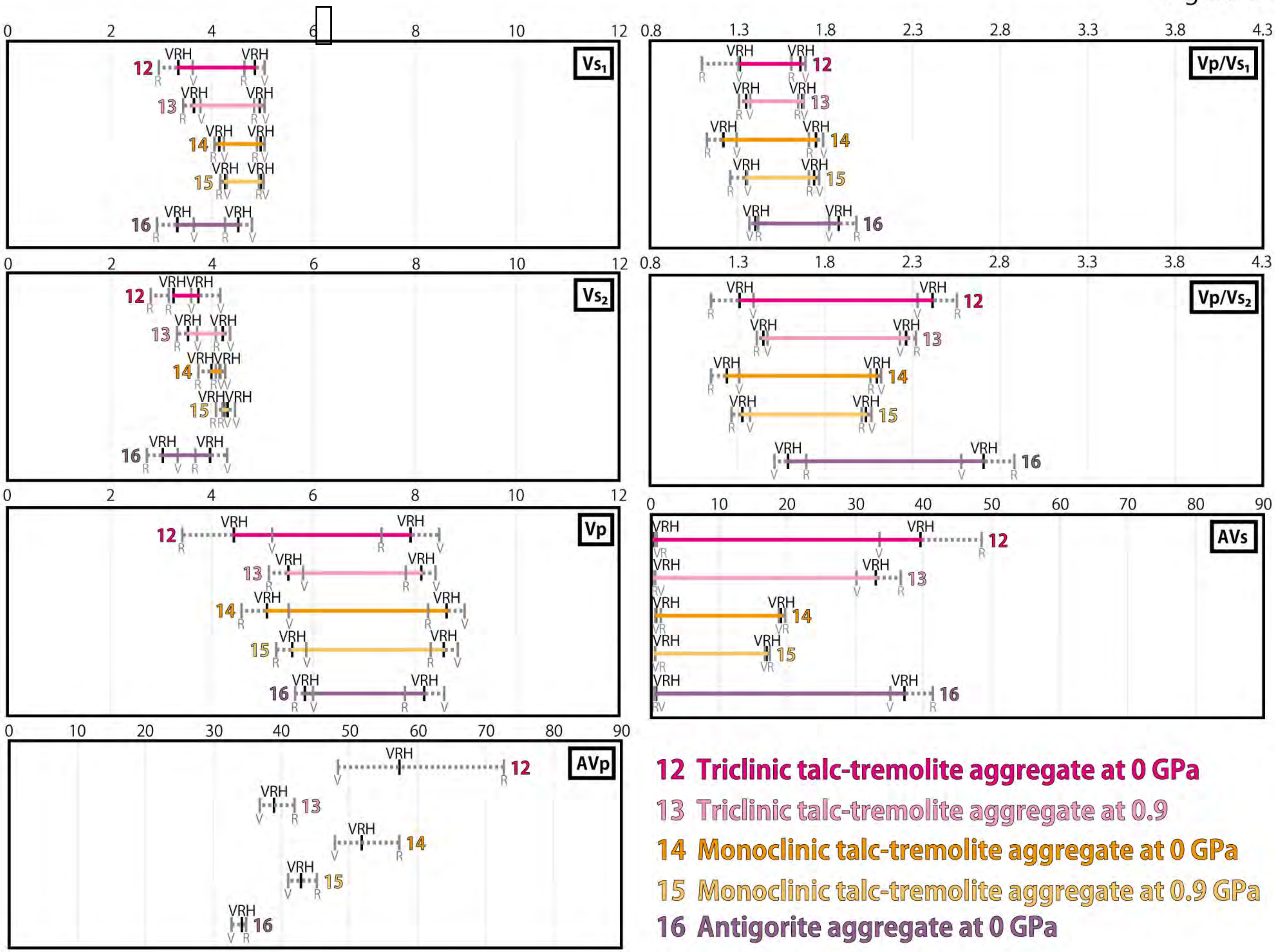

Vs1
Vp/Vs1
Vs2
Vp/Vs2
Vp
AVs
AVp
VRH
12 Triclinic talc-tremolite aggregate at 0 GPa
13 Triclinic talc-tremolite aggregate at 0.9
14 Monoclinic talc-tremolite aggregate at 0 GPa
15 Monoclinic talc-tremolite aggregate at 0.9 GPa
16 Antigorite aggregate at 0 GPa

Figure 13

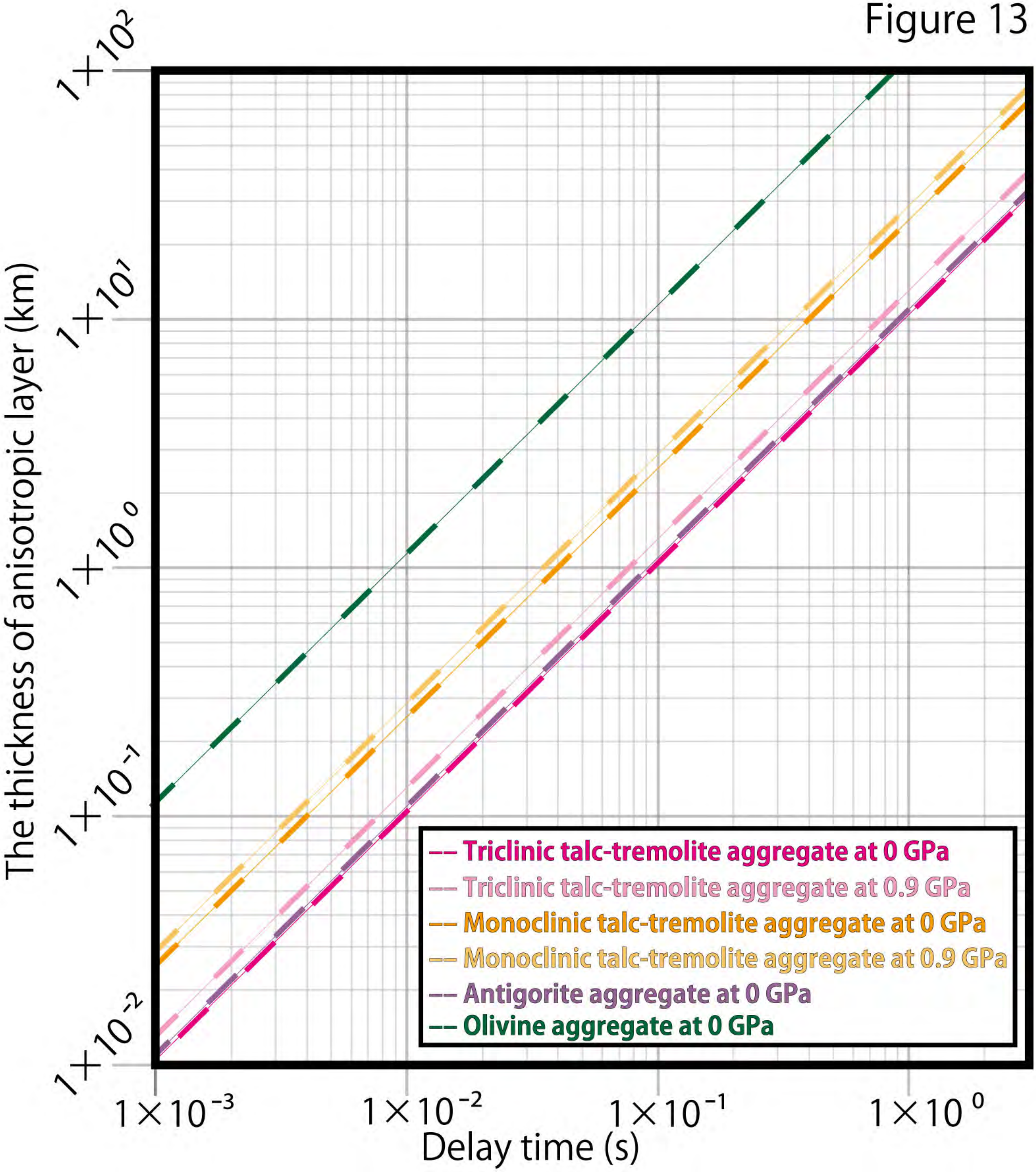

The thickness of anisotropic layer (km)
1×10²
1×10¹
1×10⁰
1×10⁻¹
1×10⁻²
1×10⁻³
1×10⁻²
1×10⁻¹
1×10⁰
Delay time (s)
Triclinic talc-tremolite aggregate at 0 GPa
Triclinic talc-tremolite aggregate at 0.9 GPa
Monoclinic talc-tremolite aggregate at 0 GPa
Monoclinic talc-tremolite aggregate at 0.9 GPa
Antigorite aggregate at 0 GPa
Olivine aggregate at 0 GPa

Table 1.

Percentage of the EBSD orientations of talc which is in close agreement (< ~20^o) with the TEM measurement for a range of different maximum MAD values.

MAD	[100]	[010]	(001)	N*
< 2.0^o	24%	27%	77%	792
< 1.8^o	25%	27%	79%	733
< 1.5^o	27%	28%	82%	631
< 1.3^o	29%	30%	85%	524
< 1.0^o	32%	32%	91%	363
< 0.7^o	32%	32%	94%	189
< 0.5^o	35%	34%	94%	71

* The number of EBSD measured points after filtering using MAD.